THREE-DIMENSIONAL MAGNETIC FIELD TOPOLOGY OF GIANT SOLAR FILAMENT

Abbi Seyoum

A Dissertation Submitted to the Department of Physics

In Partial Fulfillment of the Requirements

for the Degree of Doctor of

Philosophy in Physics

(Astrophysics)

Addis Ababa University

Addis Ababa

Ethiopia

June 2018

Addis Ababa University

School of Graduate Studies

Department of Physics

This is to certify that the thesis prepared by *Abbi Seyoum*, entitled: *Three-dimensional Magnetic Field Topology of Giant Solar Filament* and submitted in partial fulfillment of the requirements for the Degree of Doctor of Philosophy in Physics *(Astrophysics)* complies with the regulations of the University and meets the accepted standards with respect to originality and quality. Signed by the Examining Committee

1. Chairperson————————————-Sign.—————Date—————
2. External Examiner——————————Sign.—————Date—————
3. Internal Examiner——————————Sign.—————Date—————
4. Advisor—————————————Sign.—————Date—————

Chair of Department or Graduate Program Coordinator

Abstract

Solar filaments are intriguing structures suspended in the solar corona at heights up to 100 Mm above the chromosphere, but they are made of chromospheric material which is one hundred times cooler and denser than the coronal material, indicating that they are thermally and pressure isolated from the surrounding environment. Studying filaments' topological magnetic field structures, magnetic energy and electric current density is crucial to know its stability, because unstable conditions can result in explosive events: flare and coronal mass ejection (CME). All the studies in the area are limited to the small scale filaments near to the size of sunspot. This study is the first to use non-linear force-free field (NLFFF) model in spherical geometry to study a gain filament (with length more than 800Mm) along polarity inversion line (PIL) where it is in weak-field region (with photospheric field region of $\approx$ 500G). Moreover, the non-linear force-free extrapolation code take uncertainties in to account in the photospheric field data which occur due to noise, incomplete inversions or azimuth resolving techniques.

Both potential field and nonlinear force-free coronal magnetic field modeling methods are applied with preprocessing of photospheric full-disk vector magnetograms from the Helioseismic and Magnetic Imager (HMI) of solar dynamics observatory (SDO) and the Vector Spectromagnetograph (VSM) of the Synoptic Optical Long-term Investigations of the Sun (SOLIS) using the optimization procedure to full-disk vector magnetograms in spherical geometry is carried-out to make the boundary data more consistent with the force-free principle. In this process the pressure gradient and gravity are neglected, and only Lorentz force is considered. However, in solar corona for the force-free condition the Lorentz force is zero, where the current density is parallel to the magnetic field.

Topological magnetic field structure of the filament is resulted from sheared arcades over the PIL. The magnetic field lines obtained from non-linear force-free extrapolation based on HMI and VSM data have good agreement though they have different structures with the magnetic field lines from potential field source surface (PFSS) model. The non-linear force-free extrapolation based on HMI data have greater total magnetic energy, free magnetic energy, and surface electric current density compared to the one from VSM data.

Acknowledgements

First of all, I would like to express my heartily felt gratefulness to my supervisor, Dr. Araya Asfaw, for his guidance, encouragements and motivations throughout my PhD work. His freindly approach motivated me to had a remarkable scientific discussions with him. I deeply appreciate him for correcting my manuscripts and thesis, which also improved my scientific writing. I am also indebted to Dr. Tilaye Tadesse for showing his interest in my work and editing parts of my thesis. His encouragements and useful discussions have been invaluable in the present work.

I am sincerely thankful to Prof. Mark Moldwin, for accepting me as a visiting scholar at Michigan University where I got an access and training to solarsoft (SSWIDL). He has a great role in providing working facilities at the univerisity. As mentor, he has taught me more than I could ever give him credit. He has shown me, by his example, what a good scientist (and person) should be. I am extremely thankful to Dr. Ward Manchester IV, for fascinating scientific discussions, continuous inspirations and for reading parts of my thesis as well. His constructive and insightful comments really motivated me a lot during my work. Special thanks to Tong Shi, PhD student at Michigan University, for all his patience, valuable discussions and interest in my work. I am very grateful for his great support and efforts, for helping me with IDL (i.e., how to write codes and apply to analyse solar data), Unix problems and for always being in a good temper.

I am also grateful to Dr. Teshome Senbeta for his encouragements, useful discussions and facilitating this PhD program. I would like also to convey my gratitude to Dilla University for providing me financial support.

I am grateful to my family members. Most importantly, I am deeply grateful to my wife Birtukan Kebebew for all her love, patience, encouragement and faithful support during the stages of this PhD.

Contents

1

Introduction

1.1 Solar Filaments or Prominences

Solar filaments are intriguing structures of the solar atmosphere. They are suspended in the solar corona at heights up to 100 Mm above the chromosphere but they are made of chromospheric material which is one hundred times cooler and denser than the coronal material, indicating that they are thermally and pressure isolated from the surrounding environment. Because of these properties they appear darker than their background on the solar disk indicating the presence of a plasma absorption process. On the other hand, they appear at the solar limb as bright features when observed in the optical or the EUV cool lines, in this case they are called Prominences. Nevertheless, both terms, filament or prominence, are often used interchangeably in the literature. Filament plasma is embedded in a magnetic environment that lies above magnetic inversion lines, denoted a filament channel. Filaments always lie between opposite polarities of the magnetic field, i.e., along polarity inversion line (PIL) [1] The PIL can be easily identified in a magnetogramas the gray area between the negative (black) and positive (white) magnetic polarities, where the longitudinal magnetic field is absent. Generally, filaments may be grouped as: active region (AR) filaments, which are located inside active regions or very close to sunspots, lie in the lower solar atmosphere [2–4] and they harbor stronger magnetic fields, quiescent (QS) filaments which include polar crown (found around the border of polar coronal holes) and intermediate filaments (found between active regions or surrounding them). Quiescent filaments are typically much larger and more stable than AR ones. The longest filaments can cover about the solar diameter, and it is called transequatorial filament Fig. (1.1). Many excellent reviews have been written about this topic, e.g., [5–11]. The magnetic field strength and orientation inside filaments has been inferred. Several models that ex-

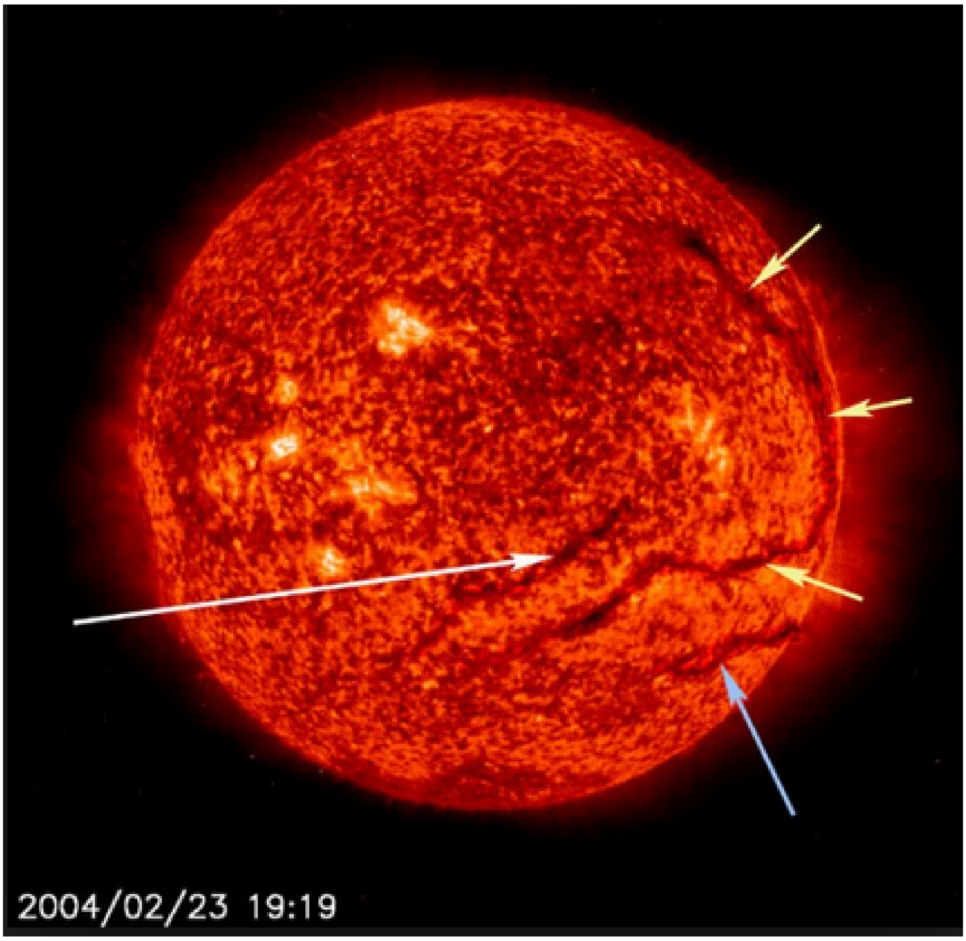

Figure 1.1: Image of the Sun as seen in the He II 304Å channel on SOHO/EIT, on 23 February 2004, revealing three dark filaments (shown by arrows). One of them extends over almost a solar diameter. Credits: ESA/NASA/EIT; Catania Astrophysical Observatory.

plain the formation mechanism and the balance of forces of these structures have been developed in the last decades. But still, many new questions have arisen recently owing to the spectacular improvement of instruments, telescopes, and numerical simulations.

This thesis will focus on three-dimensional magnetic field topology of giant solar filament, which will be analyzed in order to understand how magnetic field structure of the filament is formed and support relatively cool plasama.

1.1.1 Historical Background

Being visible during eclipses, prominences have been known for a long time. However, only during the eclipse of 1860, when photography was introduced for the first time, were prominences finally recognized as solar features and not an effect of the Earths atmosphere [12]. In the following years spectroscopy started to develop; during the eclipse of 1868 the yellow D_3 line at 5877Å was observed for the first time in prominences, later identified as coming from solar He emission [13]. Further advances in prominence knowledge and spectroscopic methods came with the discovery that prominence emission could be observed outside the limb even during daylight [14] with coronagraphs.

In the 1890s the observations of filaments on the disk with spectroheliographs began, and the first systematic photometric measurements in prominences were made by Schwarzschild in 1906. Lyot developed the coronagraph in 1936, ushering in a new era in which systematic prominence limb observations can be made outside of eclipses [15]. The first studies relating prominences to the solar cycle were published in [16] and [17]. Further information on historical prominence observations can be found in [5, 18] and references therein. Daily images of the Sun from the ground and from space are available today. They allow us to fully record solar activity in all structures, including filaments/prominences. These observations are presented in the next Section (1.2).

1.1.2 Motivations for Solar Filament Study

Decades of study have shown that it is very difficult to characterize filament properties. Filaments show differences in morphology, lifetime, position on the solar disk, complexity of their magnetic field environments, etc. They are not uniform in shape and show a fine, dynamic structure at the limit of the instrumental resolution. This high variability results in a wide range of physical conditions deduced from observations that poorly constrain the models of filament formation and their disappearance [19].

Generally, support and stability, mass motion, radiative losses, magnetic field, formation and disappearance of filaments are still unsettled issues motivating their studies. Therefore, understanding the origin of such variety and attaining better knowledge of these structures and their environment during the different phases of their life can provide valuable information on the physics of the solar atmosphere, and hence, provide valuable knowledge on flares and CME that affect both solar and Earth's atmosphere.

1.2 Filament Observations

Filament material is made almost completely of hydrogen and helium like the rest of the Sun. Due to their low temperature, filaments abound in neutral or low ionization charge states. They are best observed in the intense H and He Lyman and Balmer lines series.

For the study of filaments, finding chromospheric spectral lines that are neither too faint nor too broad, and have measurable polarization signatures is not an easy task. The most popular chromospheric spectral lines are the H_α line at 6563Å, the He I 10830Å triplet, the D_3 line of He I at 5876Å, the three Ca II lines in the 8542Å spectral region, the Ca II H line at 3968Å and the Ca II K line at 3934Å. However, it is also essential to study the photosphere below filaments using the two Fe I lines at 6301.5 and 6302.5Å or the Si I line at 10827Å. Moreover, The spectral range around the helium 10830Å triplet offers a unique opportunity to study simultaneously the chromosphere and the photosphere. The main obstacles in observing magnetic fields in chromosphere [20] are:

(1) the chromosphere is an inhomogeneous layer whose structure has to be taken into account when interpreting magnetograms,

(2) some chromospheric lines are blended by photospheric lines which affects the final magnetic field measurements,

(3) the chromosphere changes very fast and hence requires high spatial and temporal resolution for its analysis, and

(4) The presence of scattring-polarization (and its modification through the Hanle effect), Chromospheric magnetic fields are weaker and therefore the polarization signals are fainter and harder to measure.

Most often, observations are taken in the strong red visible Balmer H_α line, be it from the ground or from space (Hinode/SOT, [21]). This long wavelength allows spatial resolutions of fractions of an arcsecond to be achieved. The H_α 6563Å observation is crucial for the effective mapping of prominences and filaments. Since the H_α spectrum is polarized [22], it was originally used to study the magnetic field strength in prominences (e.g., [23, 24]). Nowadays, it is mainly used to study their morphology [26], fine structure and evolution [27,28], and Doppler shifts [29,30].

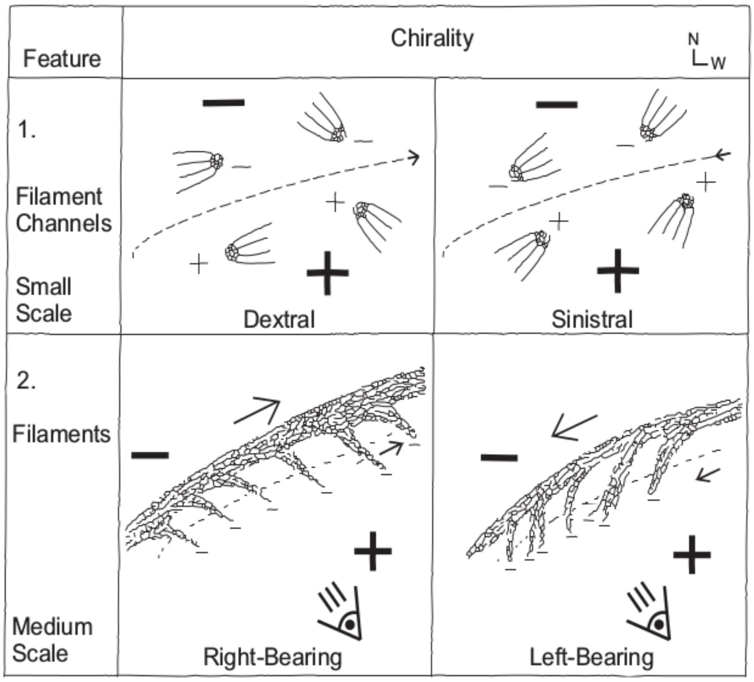

Figure 1.2: Upper row: H_α fibrils aligned with the PIL forming a filament channel. Lower row: relation between the direction of the barbs that extend from the filament and the global polarities found on each site of the filament. This figure originally appears in [25].

The H_α line is optically thick most of the time during filament observation on the disk. For this reason, by scanning the line at different wavelengths it is possible to image different plasma layers: the filament is seen at line center, while at about 0.5Å away from this position we see the chromospheric fibrils below it.

The filaments seen in H_α are also located above PILs [31]. They usually appear to be composed of a spine and barbs. [32] defined the spine as the horizontal fine structure along the long axis of the filament and the barbs as extensions along the sides of the filament, protruding from the spine. [33] investigated chromospheric fibrils around PILs. He found that the fibrils tended to align with what would become the long axis of the filament before it formed, i.e., parallel to the PIL (upper panels in Fig. 1.2). Based on H_α images, [34] concluded that filaments were formed in filament channels. However, [35] highlighted that a filament channel does not necessarily have a filament above it.

From H_α images a chirality property for filaments and filament channels has been inferred [36]. As a result, when filaments are seen from their positive polarity side, one can find right-bearing and left-bearing filaments. In the former type, the barbs extend from the spine and point to the right, while in the left-bearing filaments the barbs point to the left (lower panels in Fig. 1.2). [36] found a correlation between the magnetic field direction along the axis of the filament and the right/left-bearing barbs. The magnetic field points (bigarrow in Fig 1.2) to the right (dextral) in right-bearing filaments and to the left (sinistral) in left-bearing filaments. According to these findings, [37] developed the chiral method and its application to solve the 180^0 ambiguity of the magnetic field orientation.

Due to the strong absorption of the H and cHe continua, filaments on disk appear as dark features when observed in the EUV below 912Å, that is in the H Lyman continuum head (504Å for He I and 228Å for He II). This property is used to investigate the opacity of the medium and derive information on the prominence mass and degree of ionization. Furthermore, the dark aspect of filaments at high temperature emission observed in this waveband may come from the lack of emission at such high temperatures [38, 39]. At wavelengths longer than 912Å filaments are often not visible on the Sun at chromospheric temperatures, meaning that their plasma is transparent to such wavelengths and that their emission is probably too faint to be measured against the disk emission.

1.3 Models of Filament Magnetic Structure

In the past few decades, many researches have been carried out in order to understand the formation, growth and eruption of solar filaments/prominences. Both ground and space observations show that filaments are embedded in magnetic fields that are highly non-potential. As the dominant component of the field lies along the filaments long axis, such non-potential fields exhibit strong magnetic shear. However, the detailed structure of these fields and the associated electric currents are not well understood. Several filament magnetic field structure models have been developed by different authors in order to explain the observed filaments. Since the aim of this thesis is to get a better understanding on the formation, support and topology of giant solar filaments, some models that are quite related to our observations have been discussed below.

1.3.1 Kippenhahn-Schlüter and Kuperus-Raadu Models

Filaments are always located above the PILs, across which signs of radial components of magnetic fields are reversed. [40] model presented a simple 2D stationary support for filaments where the magnetic structure presented by Kippenhahn-Schlüter (KS) corresponded to horizontal magnetic field lines which were able to support the plasma. The basic magnetic structure is the arcade field and the dip structure is formed by the weight of condensations. This model agreed with the observations at the time (e.g., [41]).

In [42] model the dip is a part of a twisted loop-like magnetic structure. After Kuperus-Raadu (KR) model [43] has found that the magnetic reconnection is triggered by the proximity of oppositely directed vertical magnetic field lines. To balance gravity, there is an upward force produced by magnetic tension. The obser-

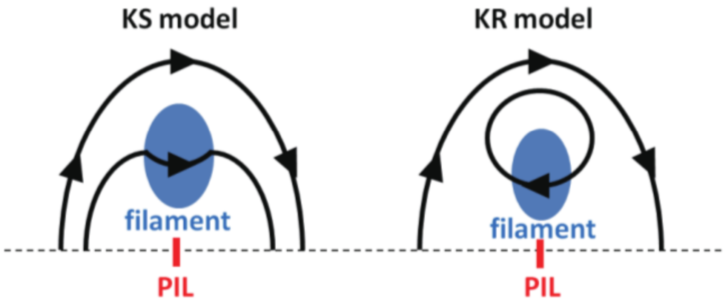

Figure 1.3: Schematic drawings of the Kippenhahn-Schlüter model and the Kuperus-Raadu model.

vational difference between KS and KR models is the magnetic polarity inside the filament relative to the ambient overlying magnetic arcade (Fig. 1.3). The KS model has normal polarity (NP) configuration (i.e., the field lines point from the positive towards the negative photospheric polarity). The KR model has inverse polarity (IP) configuration (i.e., the field lines point from the negative towards the positive photospheric polarity). The statistical study shows that both normal and inverse polarity filaments are existing in the solar atmosphere [44].

1.3.2 Sheared Arcade Model

A sheared magnetic arcade are formed by shearing motions of the magnetic field connected to dipole located below the photosphere, localized around the PIL [45, 46]. Numerical models of filament-channel formation mechanism began with a simple bipole embedded in a larger scale background dipolar field, subjected to strong footpoint motions, parallel to the PIL [47]. These oppositely directed flows drag the innermost portion of the bipole into a zone of weaker overlying field, yielding elongated, low-lying field lines that bulge upward at their less constrained ends and hence become dipped in the middle of the loop. In Fig. (1.4): the dipped field lines are the red lines with an inverse polarity (IP), field lines that carry the prominence plasma, and the overlying green field lines, coronal arcades, have normal polarity (NP).

The filament dips can be extended which corresponds to feet, or barbs [49]. Since these lateral extensions are located in dipped arcades, their chirality is opposite to the one present in flux rope.

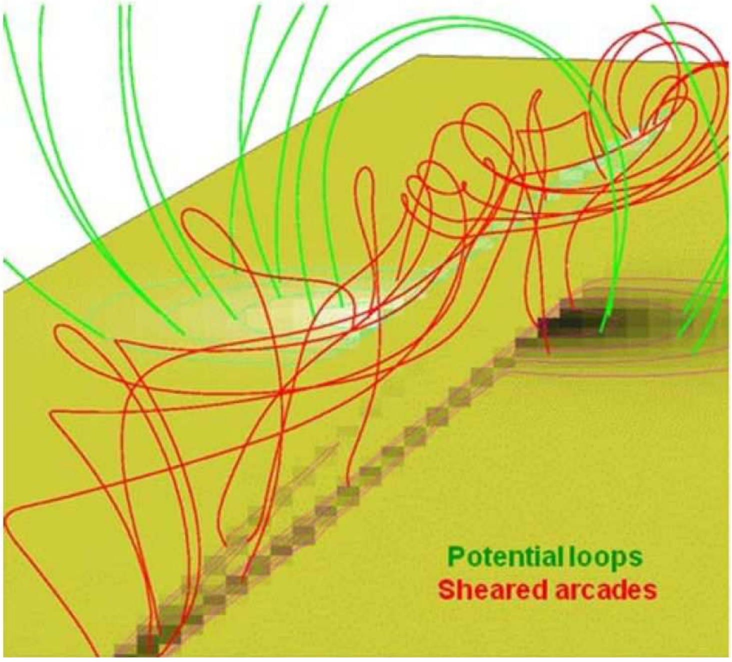

Figure 1.4: A sketch shows the sheared arcade model for magnetic field lines. Sheared arcade is shown in red colour lines and green lines represent the coronal arcade field lines. The image is adapted from [48].

1.3.3 Flux Rope Model

Magnetic flux ropes can be formed by magnetic reconnection of stressed arcades in the corona, and bodily flux emergence from below the photosphere.

In reconnection model, the formation of flux rope, twisted magnetic field lines, that support filaments or prominences was presented by [50]. The authors introduced the model for the formation of filaments through the flux cancellation by considering the shear motions (which could be due to differential rotation on the Sun) in a bipolar configuration. In this model a flux rope results from a potential field that is sheared along the PIL. That is the footpoints of the field lines experience motions converging towards the PIL. This structure eventually reconnects with other sheared field lines to produce small and large loops. The small loops submerge in to the solar surface because of their small radius of curvature which possess stronger tension force, and magnetic buoyancy prevents the submergence of large loops because of its radius resulting in smaller tension force (Fig. 1.5 a-f). This process repeats many times to build a long helical structure in corona. The dipped magnetic field lined carry the plasma and higher to the corona for the formation of filaments. [51, 52] presented about converging and shearing motions of different polarities,

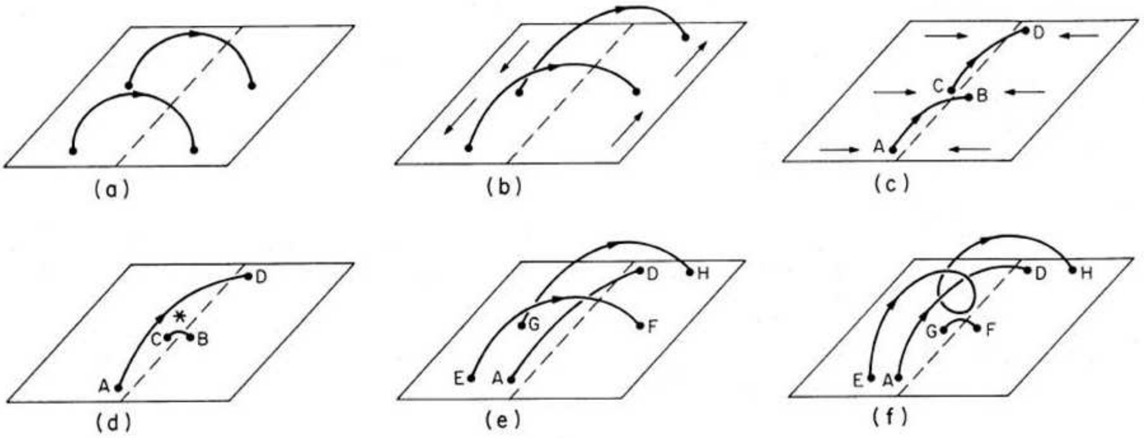

Figure 1.5: The flux rope formation model by [53] is shown. The initial configuration in panel (a) has potential field lines (solid lines) that cross the PIL (dashed line). Shearing motions and convergence towards the PIL in panels (b) and (c) trigger magnetic reconnection and finally, in panel (f), generate a flux rope. Small loops, points G and F in panel (f), that are perpendicular to the PIL have appeared and submerge below the photosphere.

rotation of sunspots, and magnetic flux cancellation twist and stretch the initial potential field gradually, leading to magnetic reconnection. If an electric current is generated in the corona, its magnetic field spreads in all directions until it meets plasma able to resist to the generated magnetic field pressure. In the low density corona, this boundary could be far away from the position of the current. Diamagnetic currents are induced at the surface of the photosphere. These induced photospheric currents are sometimes referred as a mirror current because they produce a magnetic field in the corona equivalent to the magnetic field of the mirror image of the coronal current with an opposite direction [42].

In the emergence model, a twisted flux tube is assumed to emerge from the convection zone due to the magnetic buoyancy effect into a preexisting coronal potential field [54–56]. Below the photosphere, the magnetic field of the flux rope is confined by the shielding oppositely directed boundary current [57, 58], which is held by a plasma pressure gradient (Fig.1.6).

[59, 60] reported that a helical flux rope was emerging from below the photosphere into the corona along the PIL under the preexisting prominence using observations obtained with the Solar Optical Telescope (SOT) on board the Hinode satellite. They proposed that this supply of a helical magnetic flux to the corona is associated with an evolution and maintenance of active region prominences. Emergence of the flux rope has been supported by few new observations [61–63]. Recently, from simultaneous observations in the photosphere and chromosphere, [63] have inferred a helical structure supporting the filaments plasma.

Many authors (e.g., [64–73]) have studed the rise of flux ropes from the convection zone into the corona using numerical simulations. [74], proposed that the flux rope rises through the convection zone owing to magnetic buoyancy (i.e., the flux rope is lighter than its surroundings). After it reaches the photosphere, density and pressure decrease sharply with height [75]. The flux rope evolves in to an Ω-shaped rope that barely crosses the photosphere, but its body stops rising just before reaching the surface (e.g., [67]) or slightly above it [76]. The flux rope lying just above the photosphere, expands laterally producing a broadening of the polarity inversion line. The larger the twist of the flux rope and the stronger the field, the more flux moves from the photosphere into the chromosphere [69]. The expanding field lines might reconnect with the overlying coronal magnetic field. Finally, reconnection below and above the formed flux rope eventually leads to eruptions, (e.g., [77]), producing a coronal mass ejection (CME).

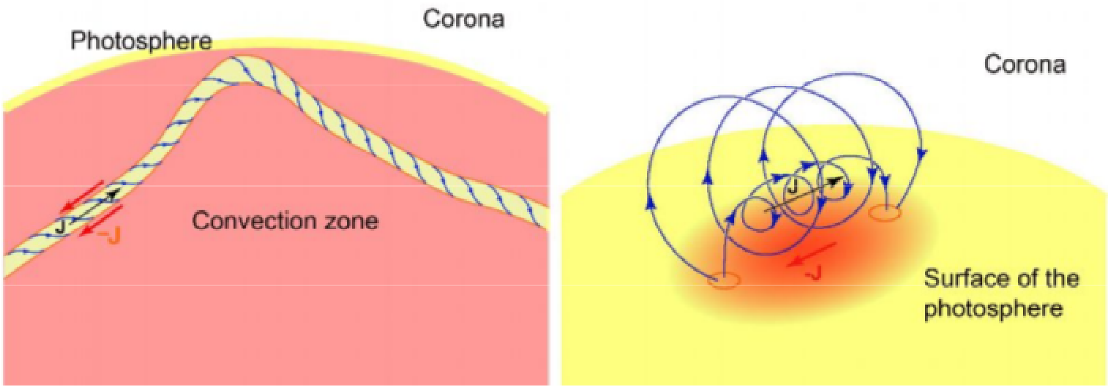

Figure 1.6: Emergence of a twisted flux tube from the convection zone into the corona.

1.3.4 Injection Model

According to injection model, cool plasma is forced to move upward in the flux tubes of a filament-channel [48, 78, 79]. The authors reported that the plasma is ejected upward due to heating or by reconnection at the base of the foot-point of the field lines (Fig. 1.7). [80] model proposed that the reconnection sites are at the PIL, while [78], suggested that the jets originate at minority-polarity intrusions off-set from the PIL. Filament barbs might be explained by the injection of cool plasma by reconnection between the filament channel field and small bipoles emerging in the channel [81–83]. Both large and small scale up-flows have been recorded in quiet-Sun filaments [84,85], although it is difficult to determine whether these flows originate at the photosphere due to spicules and other obscuring chromospheric activity. An observation made by SOT revealed that the strong jetting through out chromospheric network occurs within filament-channels on field lines and capable of hosting filament materials [86].

On the other hand, there are a few unclear properties on injection model. These include: whether injection can account for all aspects of the observed dynamic evolution of quiet-Sun prominences, whether cancellation reconnection preferentially occurs in or below the chromosphere, and heating at the footpoint which was discussed by many researchers [87–89] is not well understood. The heating length is smaller than the length of the loop [90], thus the plasma can cool down in the middle of the loop where heating is almost negligible [91–93].

1.3.5 Extrapolation

Obtaining the magnetic field structure in the solar atmosphere by measurement or theoretical calculation is one of the most important tasks to improve our understanding of physical processes in the solar atmosphere [94]. The measurement of fields throughout the coronal volume is an intrinsically more difficult problem since it requires three dimensional information, whereas photospheric fields are measured on a two dimensional surface. The techniques used to measure magnetic fields in the photosphere rely on Zeeman splitting and Stokes profile measurements and are not as effective in the solar corona, since lines formed at coronal tempera-

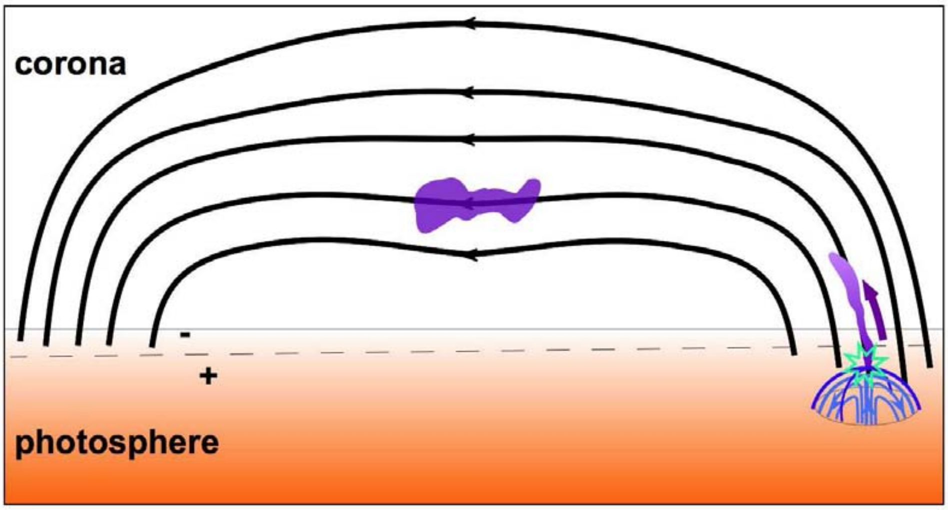

Figure 1.7: A sketch of an injection model, prominence plasma is shown in purple colour, heating is in blue colour and black lines are the filament channel field lines. Dashed line indicates the PIL. Figure adopted from [48].

tures are intrinsically broader and are scarce in the infrared where Zeeman splitting is (relatively) large. Alternatively, the Hanle effect on ultraviolet emission lines can be used to measure the coronal magnetic field but this requires space-based observations. In particular, [95] used the He I 1083 nm multiplet and [96] used the HI $L_{y\alpha}$ and $L_{y\beta}$ lines to test their ability to probe the coronal magnetic field. Coronal emission lines at optical frequencies are very faint and extremely broadened due to the low coronal plasma density and the high temperature of emitting ions, respectively.

The measurement techniques applicable to the lower layers of the solar atmosphere can also be applied to measure magnetic fields at somewhat greater heights (e.g., [97]). Using the boundary conditions being taken to be the measured values of the magnetic field in the denser and cooler photosphere, we can infer the coronal magnetic field. Therefore, the extrapolation of magnetic field measurements taken at photosphere (and/or chromospheric) level into the corona to get an estimate of the coronal magnetic field is an essential tool for solar physics [98–123].

For the extrapolation of photospheric magnetic fields into the corona, we have to solve the following questions: does the boundary condition of the magnetic field on the photosphere suffice for a unique solution in the corona with a proper asymptotic behavior at infinity? What are contributions of electric currents in the corona to its magnetic field distribution? Such questions cannot be answered in a simple way which leaves the door open to approximations and a priori assumptions in making physical models of the system (photosphere to corona) to compute coronal magnetic fields [124].

The most commonly used magnetic field extrapolation (or reconstruction) methods rely on various assumptions of the solar corona which include: the coronal magnetic field is in equilibrium ($\partial/\partial t \approx 0$) and plasma flow can be neglected, plasma densities are small, thus the Lorentz force greatly exceeds the gravitational force, the ratio of thermal pressure to magnetic pressure (the plasma β) in the corona is small, and the corona structures change on length scales comparable to or shorter than the typical coronal scale height. Therefore, the ideal magnetohydrodynamic (MHD) equations relevant for the extrapolations are reduced to:

$$\mathbf{J} \times \mathbf{B} = 0 \tag{1.1}$$

$$4\pi\mathbf{J} = \nabla \times \mathbf{B} \tag{1.2}$$

$$\nabla \cdot \mathbf{B} = 0 \tag{1.3}$$

where, **J** is a current density and **B** is the magnetic field. From Eq. (1.1) we see that the current density is parallel to the magnetic field. Therefore,

$$4\pi\mathbf{J} = \alpha\mathbf{B} \tag{1.4}$$

where, α is the force-free parameter, and it is a function of position but remains constant along each field line. It gives information of the level of twist of the field line. Eq. (1.2) can be written as

$$\nabla \times \mathbf{B} = 0 \tag{1.5}$$

The three different force-free magnetic field extrapolation are potential ($\alpha = 0$), linear force-free (α is constant and unique value for all field lines), and non-linear force-free (α varies from field line to field line but remains constant along each field line). All these methods of magnetic field extrapolation are briefly discussed in Chapter 3.

1.4 Magnetic Field Measurements

1.4.1 Polarimetry

An electromagnetic (EM) wave such as light always consists of a coupling oscillating electric field and magnetic field which are perpendicular to each other and perpendicular to the direction of propagation. If the electric field vector of a group of EM waves oscillates in an organized way we say that the light is polarized. By convention the polarization of EM waves refers to the direction of electric field. The components of an electric field vector in x-y plane can be given as

$$E_x = E_1 cos(\omega t - \phi_1), \quad E_y = E_2 cos(\omega t - \phi_2) \tag{1.6}$$

where, E_1 and E_2 are constants representing the amplitude of the wave, ω is the angular frequency, t is the time coordinate, and ϕ_1 and ϕ_2 are the phases of each component. The amplitudes of the wave (E_1, E_2) together with the phase difference between E_x and E_y , i.e., $\phi_1 - \phi_2$, describe the polarization state of the wave: linear, circular or elliptical. Thus, when both phases have the same value $\phi_1 = \phi_2$, the electric field vector $\boldsymbol{E}$ follows a straight line in the x–y plane, the light beam is linearly polarized. The circular polarization state (a circle is traced out by the electric field vector in the x–y plane) is achieved when the components have their phases shifted by $\pi/2$ (or $3\pi/2$), i.e., $\phi_1 - \phi_2 = \pm 90°$, and their amplitudes are the same. If none of the previous cases apply, the light is elliptically polarized. Although the electric field is not directly measured, we can make a measurement from an observation of superposition of many wave packets. This can be done using Stokes parameters: I, Q, U and V, which are average of the amplitude and phase $\boldsymbol{E}$:

$$\begin{aligned} I =< E_1^2 + E_2^2 >, \quad Q =< E_1^2 - E_2^2 > \\ U =< 2E_1E_2cos(\phi_1 - \phi_2) >, \quad V =< 2E_1E_2sin(\phi_1 - \phi_2) > \end{aligned} \tag{1.7}$$

In Eq. (1.7) I is the total intensity and Q is the intensity difference between horizontal and vertical linear polarizations. Stokes U gives information about the intensity difference between linear polarization at $+45^0$ and 45^0 and Stokes V allows us to distinguish between right or left-handed circular polarization. The advantage of these parameters is that a polarimeter, installed at the telescope, is able to measure linear combinations of time averages of the four Stokes parameters.

A polarimeter is an instrument that can measure linear combinations of the Stokes I, Q, U , and V parameters. The basic properties of the Stokes parameters are:

$$I^2 = Q^2 + U^2 + V^2 \tag{1.8}$$

for purely monochromatic coherent radiation, and

$$I^2 \geq Q^2 + U^2 + V^2 \tag{1.9}$$

for non-coherent radiation.

Two fundamental components of a polarimeter are the polarizer and the retarder (e.g., [125, 126]). When the light beam reaches the polarizer, only the component of the electric field vector oscillating along a particular axis will pass through it.

If the electric vector oscillates perpendicular to that axis, then the polarizer is completely opaque to that light. Therefore, a desired polarization state of the incoming light beam (e.g., linear at 90^0) can be selected. On the other hand, a retarder divides the incident beam into two orthogonal components and shifts the phase of one of them with respect to the other. As the result, the polarization state can be modified. Once the radiation goes through the retarder and polarizer (see the scheme in Fig. 2 by [125]), the output beam $I_{out}(\alpha, \phi)$ is a linear combination of the four Stokes parameters, where α is the angle of the transparent axis of the polarizer with respect to an arbitrary reference axis and ϕ is the phase shift introduced by the retarder. Several variations of α and ϕ yield different measurements of $I_{out}(\alpha, \phi)$. A combination of the obtained $I_{out}(\alpha, \phi)$ leads to the determination of the Stokes parameters. In particular, Stokes Q, U , and V are calculated combining several $I_{out}(\alpha, \phi)$ measurements.

The optimization of modulation efficiency of the polarimeter at the wavelengths of the two chromospheric He I lines is therefore of primary importance. As it turns out, the polarimeter is fairly achromatic, with good levels of modulation efficiency anywhere between 570 nm and 1200 nm. This fact allows the investigation of other important chromospheric lines, like the Na I D doublet (589.3 nm), H_α (656.3 nm), and the Ca II IR triplet (849.8nm, 854.2nm, 866.2nm), as well as the forbidden coronal lines of Fe XIII (1074.7nm and 1079.8nm). In particular, H_α adds the possibility of plasma density diagnostics through the modeling of the net circular polarization induced by the micro-turbulent electric plasma fields [127].

1.4.2 Zeeman Effect

Zeeman effect is named after Dutch discoverer, Pieter Zeeman in 1896, who began to study the effect of an external magnetic field on light. He noticed that spectral lines split under the influence of the field though he could not fully explain the phenomenon (due to the fact that quantum physics had not yet been devised), he was able to prove the theory of electromagnetic radiation put forth by Lorentz.

The magnetic field of the Sun can be probed in a rather precise and direct manner because in the presence of a magnetic field the energy levels of atoms (and ions and molecules) are split into more than one level. This causes spectral transition lines to split into more than one line, with the amount of splitting proportional to the strength of the magnetic field. This is called the Zeeman Effect, and the corresponding increase in the number of spectral lines is called Zeeman splitting. Thus, we can infer the presence of magnetic fields if we observe Zeeman splitting in the spectrum, and we can measure the strength of the field by measuring quantitatively the amount of Zeeman splitting.

In quantum mechanics, a shift in the frequency and wavelength of a spectral line implies a shift in the energy level of one or both of the states involved in the transition. The Zeeman effect that occurs for spectral lines resulting from a transition between singlet states is called the normal effect, while that which occurs when the total spin of either the initial or final states, or both, is nonzero is called the anomalous effect.

In the normal Zeeman effect the electron spins cancel each other in both the initial and final state and the energy of an atomic state in a magnetic field depends only on the magnetic moments of the electron orbit. The energy difference, ΔE

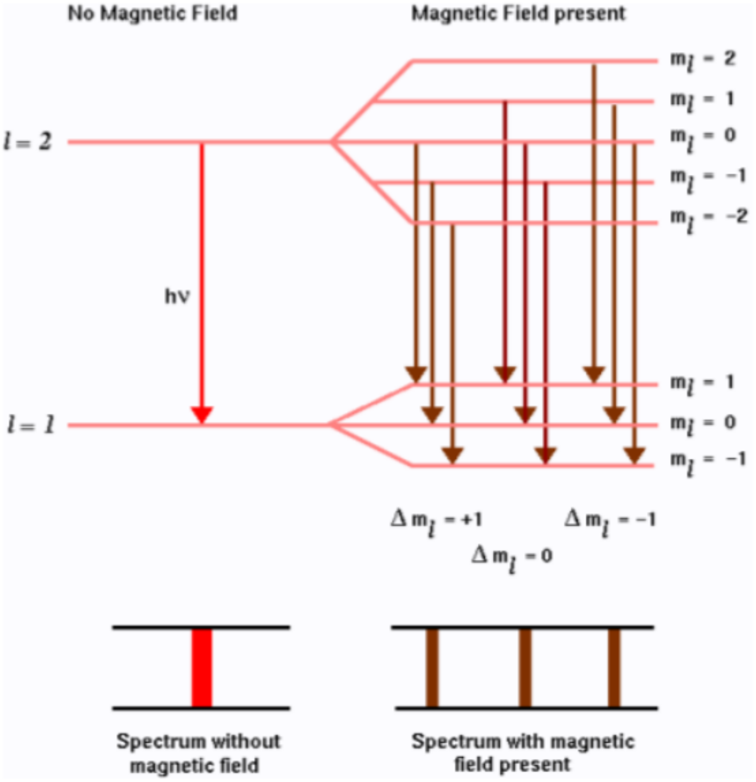

Figure 1.8: Zeeman Effect.

which occurs as a result of magnetic field applied to the orbital magnetic moment can be given as

$$\Delta E = m_l \mu_B B \tag{1.10}$$

This energy gap is what causes the Zeeman Effect. Each value of l has $2l + 1$ values of m_l associated with it. Thus, when an external magnetic field is turned on, the electrons with the same value for l split into their different values for m_l , raising or lowering their total energy as described in Eq.(3.5). Transitions are governed by the following transition rules

$$\Delta l = \pm 1 \tag{1.11}$$

$$\Delta m_l = 0, \pm 1 \tag{1.12}$$

Because of the uniform splitting of the levels, there are only three different transition energies. The central line, with $\Delta m_l = 0$, is called the main line or the π line, and the lines for which $\Delta m_l = \pm 1$ are the satellites or σ lines. The π spectral line is polarized parallel to the magnetic field lines, and the σ lines are polarized perpen dicularly to the magnetic field lines.

The anomalous Zeeman effect occurs when the spin of either the initial or the final states, or both, is nonzero. For this type of Zeeman effect the magnetic moment due to spin is 1 rather than $\frac{1}{2}$, and as a result the total magnetic moment is not parallel to the total angular momentum. The total change in energy is given by

$$\Delta E = g m_j \mu_B B \tag{1.13}$$

where g is called the Land$\acute{e}$ g factor, which is given by

$$g = 1 + \frac{j(j+1) + s(s+1) - l(l+1)}{2j(j+1)} \tag{1.14}$$

Each energy level is split into $2j + 1$ levels, corresponding to the possible values of m_j, and there are more than three different transition energies due to the fact that the upper and lower states are split by different amounts and purely quantum mechanical [128]. As expected, for $s = 0$, $j = 1$, and $g = 0$ in Eq. (3.7) gives the splitting in the normal Zeeman effect. When spin is taken into account, the transition rules are:

$$\begin{aligned} \Delta j &= 0, \pm 1 \\ \Delta m_j &= 0, \pm 1 \end{aligned} \tag{1.15}$$

It is important to note that the π component $(\Delta m_j = 0)$ is not displaced in wavelength, while the σ components $(\Delta m_j \pm 1)$ are shifted symmetrically to the red $(\sigma_r$ for $\Delta m = +1)$ and and blue $(\sigma_b$ for $\Delta m = -1)$ of the original wavelength. When the magnetic field $\boldsymbol{B}$ is oriented parallel to the observers line-of-sight (LOS), only the σ transitions of the spectral line are seen and are circularly polarized while no π transitions are seen (longitudinal Zeeman effect). The circular polarization spectrum shows two antisymmetric lobes (see e.g., Fig.1 in [129]). Longitudinal magnetograms are based on this effect and are extremely useful to obtain 2D images of the Sun showing the longitudinal component of $\boldsymbol{B}$. When $\boldsymbol{B}$ is perpendicular to the LOS, both π and σ components can be measured and represent linearly polarized light (transverse Zeeman effect). The linear polarization spectrum shows one central lobe (π component) and two symmetric lobes placed on each side (σ_b and σ_r). However, usually $\boldsymbol{B}$ is neither completely longitudinal nor transverse with respect to the LOS and therefore has certain inclination and azimuth.

1.4.3 Hanle Effect

The Hanle effect have revealed the existence of vast amounts of hidden magnetic flux in the solar atmosphere which remains invisible to the Zeeman effect due to cancellations inside each spatial resolution element of the opposite-polarity contributions from this small-scale, tangled field. It is the modification of the atomic level polarization (and of the ensuing observable effects on the emergent Stokes profiles Q and U) caused by the action of a magnetic field inclined with respect to the symmetry axis of the pumping radiation field. In the presence of an inclined magnetic field that breaks the symmetry of the scattering polarization problem, forward scattering processes can produce linear polarization signals in spectral lines. In this case, the linear polarization is created by the Hanle effect, a physical phenomenon that has been clearly demonstrated via spectropolarimetry of solar coronal filaments in the HeI 10830Å multiplet [130].

The magnetic field intensity, B (measured in gauss), sufficient to produce significant change in the atomic level polarization results from equating the Zeeman splitting with the natural width (or inverse lifetime) of the energy level under consideration:

$$2\pi\nu_L g = 8.79 \times 10^6 B g \approx 1/t_{life} \tag{1.16}$$

where ν_L is the Larmor frequency, g is Land$\acute{e}$ factor and t_{life} is lifetime (in seconds), which can be either the upper or the lower level of the chosen spectral line. This relation shows that the Hanle effect allow us to diagnose stellar magnetic fields having intensities between milligauss and a few hundred gauss which is very hard to study via the Zeeman effect alone. It is therefore clear that the Hanle effect is an important diagnostic tool to study structures that involve weak fields in the solar atmosphere.

[131] presented that reliable Hanle-effect diagnostics can be achieved by means of three dimensional (3D) multilevel scattering polarization calculations in snapshots taken from realistic simulations of solar surface convection (see [132, 133]). These radiation hydrodynamical simulations of the photospheric physical conditions are very convincing because spectral synthesis of a multitude of iron lines shows remarkable agreement with the observed spectral line profiles when the meteoritic iron abundance is chosen [134].

1.4.4 Inversion

In radiative transfer equation, inversion codes are the best tool available to infer the physical properties of the solar atmosphere. Although these inversion codes have been used successfully in multiple investigations (see reviews by [135–138]), they do not adequately address the questions of convergence and uniqueness. This has led many researchers to rely on simpler methods in their investigations: separation between $I+V$ and $I-V$ to determine the line-of-sight component of the magnetic field [139, 140], center-of-gravity or bisector analysis to find the line-of-sight component of the velocity [141, 142], separation of σ components in Stokes I to get the total magnetic field strength [143, 144], weak-field approximation to determine the magnetic field vector [145].

The main idea of any Stokes inversion code is to iteratively fit the observed Stokes vector at each wavelength position $I^{obs}(\lambda) = (I, Q, U, V)$. This fit is done by producing a synthetic Stokes vector $I^{syn}(\lambda, M)$, that it is then compared at each wavelength position with the observed one via the χ^2 of the fit:

$$\chi^2 = \frac{1}{4L - F} \sum_{i=1}^{L} \sum_{j=1}^{4} \left[I_j^{obs}(\lambda_i) - I_j^{syn}(\lambda_i, M) \right]^2 \frac{\omega_{ij}^2}{\sigma_j^2} \tag{1.17}$$

where L is the number of wavelength points observed ($L = 6$ in HMI's case) and F is the number of free parameters. Therefore, $4L - F$ refers to the number of degrees of freedom in the inversion. $I_j^{obs}(\lambda_i)$ and $I_j^{syn}(\lambda_i, M)$ refer to each of the four Stokes parameters, σ_j refers to noise level, ω_{ij} refers to weighting function and M indicates synthetic profiles that depend on series of model parameters.

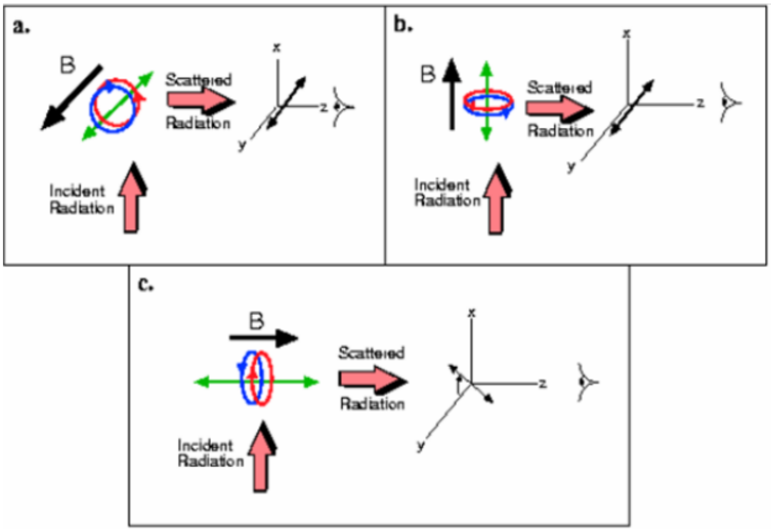

Figure 1.9: Hanle Effect in scattering.

Nowadays, Inversion codes for the radiative transfer equation are used in order to analyze many data pipelines for space-borne and ground-based instruments. That is the case of Hinode/SP [146], SDO/HMI [147], and SOLIS/VSM [148]. We have applied the most widely used inversion codes, called Milne-Eddington (M-E) codes that solve the radiative transfer equation under the M-E approximation [149]. Although M-E codes operate under restrictive assumptions about the thermodynamics of the solar plasma, they are often regarded as being able to retrieve reliable values for the magnetic and kinematic properties of the solar photosphere, and even chromoshere [150].However, the interpretation of M-E inferences is not straightforward, as the Milne-Eddington solution for the radiative transfer equation assumes that the magnetic field and velocity are constant with height through the solar atmosphere.

1.4.5 Resolving 180^0 Ambiguity

From polarimetric observations it is possible to infer the vector magnetic field B. However, complications occur when the observed region is far away from the disk center and consequently the line-of-sight and vertical magnetic field components are far apart (see [151], for details). The inverted horizontal magnetic field components cannot be uniquely derived, but contain a 180^0 ambiguity in azimuth, which has to be removed before the fields can be extrapolated into the corona.

This ambiguity is attributed to the fact that the polarization signal due to the transverse field component provides only the plane of linear polarization. Using the linear polarization of magnetically sensitive spectral lines to determine the field perpendicular to the line-of-sight results in an ambiguity of 180^0 in its direction [152].

There is no known method for resolving the ambiguity through direct observation using the Zeeman effect, unless some a priori assumptions regarding the structure of the magnetic field vector are used (e.g., regarding smoothness). Some methods require an approximation regarding the 3D magnetic field structure (usually from a potential field extrapolation); for example to minimize the divergence of magnetic field vector or the angle with respect to the potential field.

Although, there is no easy way to solve this problem, several methods have been used to address this issue (see [153], for a complete review on this issue). Among others: the Improved Acute Angle method [154, 155], the Minimum Energy method (e.g., [156]), the Magnetic Pressure Gradient [157], the Uniform Shear method [158], the Structure Minimization method [159], the AZAM Utility (see Appendix A in [160]) and the Chiral method [161]. A description of each of them is far beyond the scope of this thesis. Nevertheless, a brief description of the Minimum Energy method utility is presented below since that code was applied to the data of this thesis.

Minimum Energy Method

The minimum energy method has been developed by [162]. As other sophisticated methods it uses the potential-field acute angle method as the initial step. Subsequently a pseudo energy, which is defined as a combination of the magnetic field divergence and electric current density, is minimized. In the original formulation the energy was defined as $E = (|\nabla \cdot B| + |j|)$, which was slightly modified to

$$\sum E = (|\nabla \cdot B| + |j|)^2 \tag{1.18}$$

in an updated version. For computing j_x , j_y , and $\partial B_z/\partial z$, a linear force-free model is computed. The method minimizes the functional (1.18) with the help of a simulated annealing method, which is a robust algorithm to find a global minimum. In a recent update (published in [163]) the (global) linear force-free assumption has been relaxed and replaced by local linear force-free assumptions in overlapping parts of the magnetogram. The method was dubbed nonlinear minimum energy method, although it does not use true NLFF fields (would be too slow) for computing the divergence and electric currents. The original linear method got a fraction of 0.98 of pixels correctly and the nonlinear minimum energy method even 1.00. Almost all pixels have been correct, except a few on the boundary. Among the fully automatic methods this approach had the best performance on accuracy. A problem for practical use of the method was that it is very slow, in particular for the nonlinear version. Minimum energy methods are routinely used to resolve the ambiguity in active regions as measured, e.g., HMI on SDO.

1.5 Outline of the Thesis

The main aim of this thesis is to improve our understanding on giant solar filament by comparing observation with theoretical models. From observed photospheric vector magnetogram, we have implemented spherical potential field source surface (PFSS) and nonlinear force-free field (NLFFF) extrapolation of a coronal magnetic field over a giant filament on the solar disk. We use full-disk or cutout HMI vector data. Using those data we have investigated the magnetic field strength, electric current density and magnetic energy, which help us to infer stability of the filament and support our efforts to improve space weather predictive capabilities. There have been extensive studies of filaments using NLFFF models (e.g., [164]). However, all these works are limited to relatively small-scale filaments (length within tens of megameters) whose channel is close to sunspots and along the main polarity inversion line (PIL) with strong transverse field and magnetic shear, and those filaments are quite smaller than the giant filament we have studied. Spherical NLFFF code have been used to investigate topological magnetic field structure of selected giant filament using currently available SDO/HMI full-disk or cutout data [124]. Although the presence of a large-scale flux rope can hardly be predicted from the noisy vector magnetogram for the giant filament, its three-dimentional magnetic field topology is modeled using HMI vector magnetograms which have been pre-processed by Schucks decontamination algorithm. Magnetic field lines of the region containing the giant filament have been reconstructed from full-disk or cutout data while it crosses the solar disk. We have compared SDO/HMI and SOLIS/VSM data models with the observation from SDO/AIA.

2

Observation and Instrumentations

The Earth receives light from the Sun at all wavelengths of electromagnetic radiation. The radiation is quite essential to study many solar features. We use both space and ground based instruments to study the solar filaments from the Earth's surface. The use of space-based telescopes is quite important to study the hotter plasma in the solar corona, particularly in solar filaments which is mainly observed in the Extreme ultraviolet (EUV), X-rays and gamma rays.

A giant filament observed on February 10, 2015 (see Fig. 2.1) is investigated under this study using observational data from Solar Dynamic Observatory (SDO)-the Helioseismic and Magnetic Imager (HMI), space-based optical instrument and Synoptic Long-term Investigations of the Sun (SOLIS)-Vector Spectromagnetograph (VSM), ground-based optical instrument for solar observation.

2.1 The SDO

The Solar Dynamic Observatory (SDO) is a NASA satellite mission. It was launched on February 11, 2010 from Cape Canaveral Air Force Station [165]. The main objectives of the SDO are to understand the 11-year solar variability, how it is generated and how the solar activity is related to the space weather, to understand the magnetic field configuration from the Sun's interior to the outside (in the corona) and to understand what drives Coronal Mass Ejections (CME), filament eruptions and flares. To achieve these scientific goals, three different instruments (AIA, HMI and EVE) have been built on SDO (see Fig. 2.2).

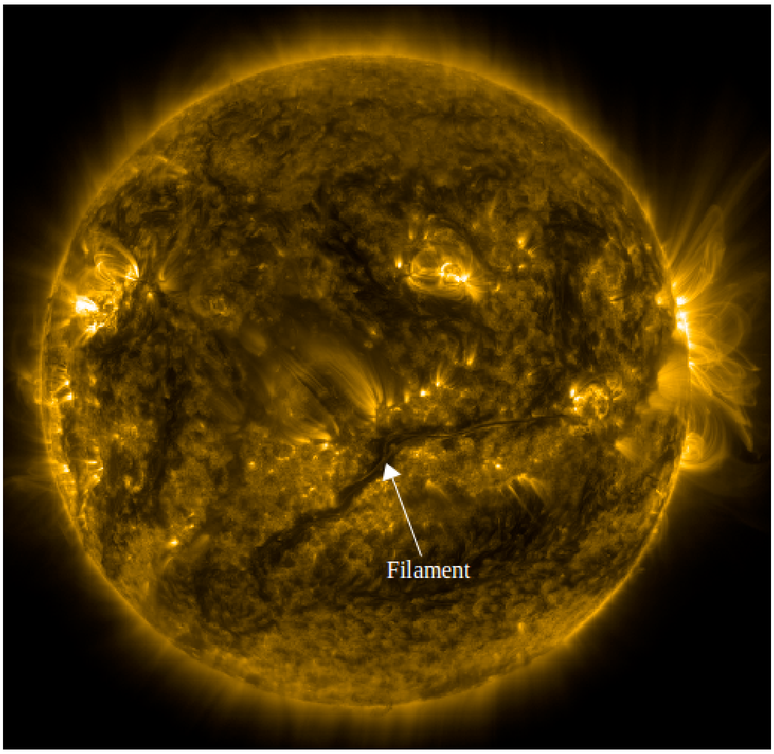

Figure 2.1: Giant filament observed on February 10, 2015 at the wavelength of 171Å using SDO/AIA. Image credit: NASA's SDO/AIA.

2.1.1 SDO/AIA

The Atmospheric Imaging Assembly (AIA) is an instrument on board of the SDO spacecraft. It began capturing data on the 27^{th} of March 2010 and has since been providing full-disc images with unprecedented resolution and cadence, revealing the breathtaking structure of the solar atmosphere in a way which has not before been seen. It observes the Sun in multi-wavelength channels to investigate a broad range of scientific objectives. For example, dynamics of coronal structures, coronal heating–what is the source of heating and coronal emission?, magnetic reconnection, origin of coronal mass ejections and how they propagate into the heliosphere.

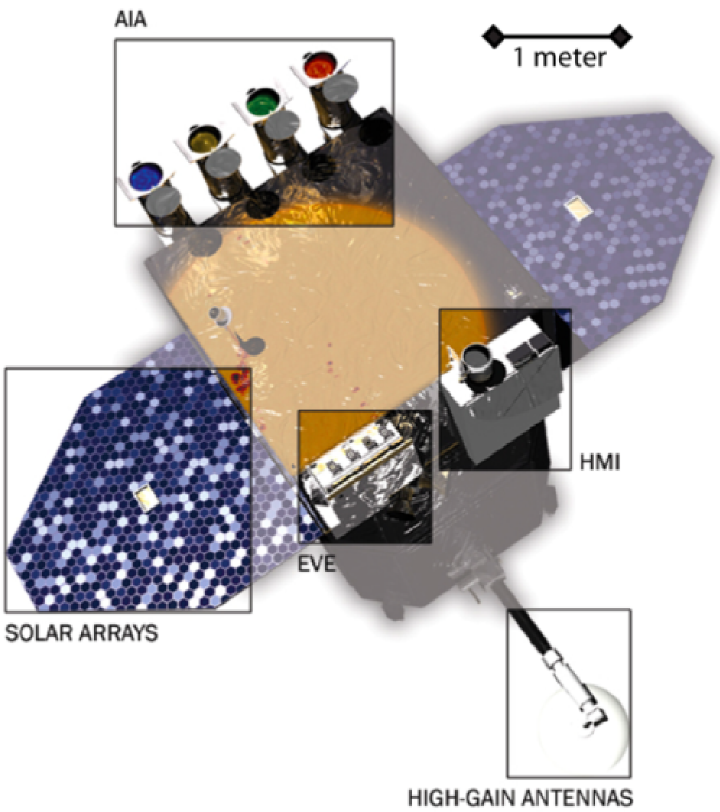

Figure 2.2: An image of the SDO spacecraft, showing its three main instruments: HMI, AIA and EVE. Solar arrays and high-gain antennas are on the left and bottom side. Image adapted from [165].

As mentioned above, AIA has been built to study the temporal evolution of the solar coronal structures [166]. To achieve this goal, AIA has been designed to take high cadence full-disk images in ten different wavelength bands, seven in EUV, two in UV and one in Visible channel as shown in Fig. (2.3). It provides high spatial resolution images of $0.6''$ per pixel of entire solar disk (4096×4096 pixel images) with a cadence of 12 seconds. The AIA is capable of taking almost simultaneous observations of the entire solar disk in wavelength bands selected to pickout structures with plasma temperatures from 10^4 to 10^7K (see Fig. 2.3).

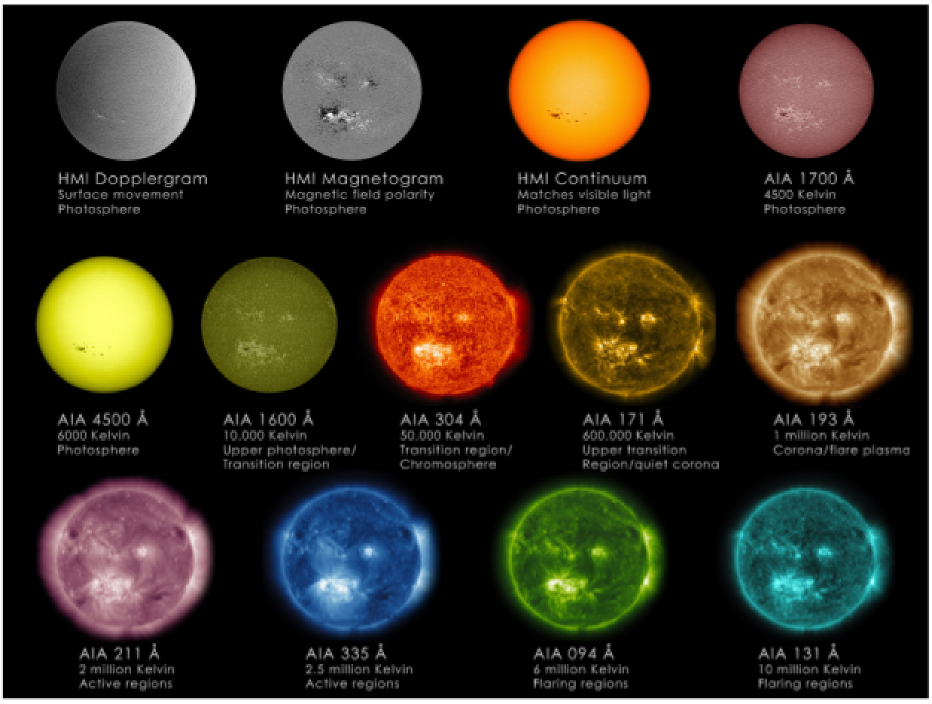

Figure 2.3: AIA images in each bandpass, as well as three HMI images. Image credit: NASA/SDO/AIA.

The AIA instrument is made up of four Cassegrain telescopes, and Each of the four telescopes is divided into two parts. Fig. (2.4) shows the schematic diagram of four AIA telescopes in different wavelength band passes. One half of telescope 3 has three selectable UV-Visible wavebands and the other half of it has 171Å wavelength band filter. The remaining three telescopes, 1, 2 and 4, have one wavelength filters on each half (see Table. 2.2). Further detailed information about the telescopes is given in the papers by [168, 169].

2.1.2 SDO/HMI

The Helioseismic and Magnetic Imager (HMI) was built at the Lockheed Martin Solar and Astrophysics Laboratory (LMSAL) in collaboration with Stanford University. It is designed to study the dynamics and origin of magnetic field on the Sun [170]. The Joint Science Operations Center (JSOC) serves both the HMI and Atmospheric

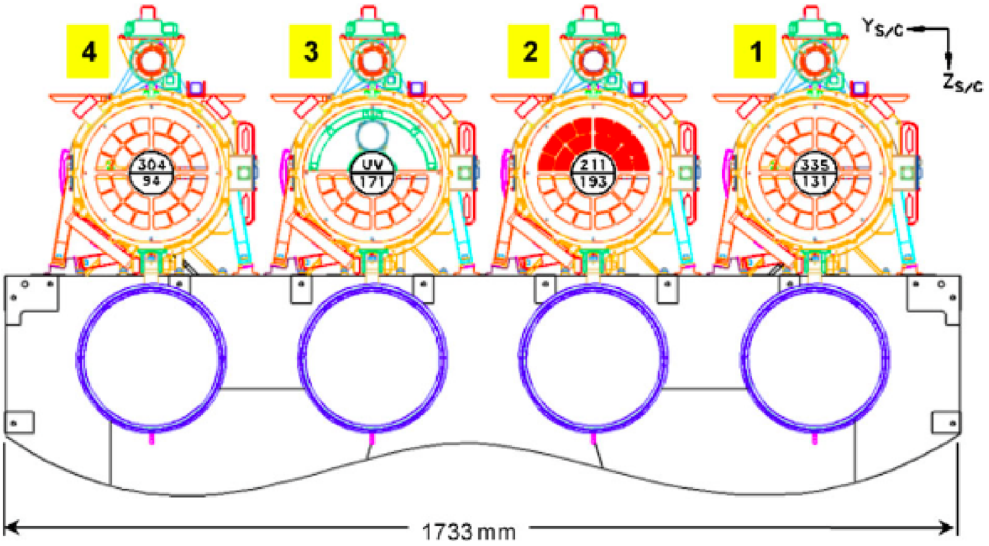

Figure 2.4: Sketch of the four AIA telescopes showing the division of wavelength bands. Each telescope is divided into two parts. The waveband of each part is shown in Table 2.2 (courtesy of [167]).

Imaging Assembly (AIA) instruments on SDO, providing pipeline processing of the incoming data products as well as archival and retrieval services for investigators who want to use the data. Extensive online documentation for the JSOC data center can be accessed [1].

HMI makes two independent measurmenents of the line-of-sight components of the photospheric magnetic field using two 4096×4096 pixel CCD cameras. Each camera records a full-disk image of the Sun every 3.75 seconds in a 76 mÅ wavelength band selected by tuning the final stage of a Lyot filter and two Michelson interferometers across the FeI 6173.34Å absorption line. The two measurements are:

i. hmi.M.45s magnetogram measure full-disk scalar quantities-Doppler shift, longitudinal magnetic field, continuum intensity, line depth, and line width-using

---

[1] http://jsoc.stanford.edu

a repeating sequence of narrow-band images recorded every 45 seconds with a 4096×4096 camera called the ″Doppler″ camera, where the difference in Dopplergrams obtained in right or left polirized light.

ii. hmi.M-720s magnetogram are computed every 12 minutes by combining registered filtergrams collects during several sequences in which the image provide a full disk low-noise image of the sun using the second identical camera called the ″Vector″ camera. The camera measures six polarization states every 135s: nominally $I \pm V$, $I \pm Q$, and $I \pm U$; where I, Q, U & V are the Stokes polarization parameters. From these the vector magnetic field and other plasma parameters can be derived.

Table 2.1: The primary ions observed by AIA and their approximate height of formation. The table is taken from [166].

Channel	Primary ion(s)	Region of atmosphere	log(T)
4500Å	continuum	photosphere	3.7
1700Å	continuum	temperature minimum, photosphere	3.7
1600Å	CIV	transition region, upper photosphere	5.0, 4.0
304Å	HeII	chromosphere, transition region	4.7
171Å	FeIX	quite corona, upper transition region	5.8
193Å	FeXII, FeXXIV	corona and hot flare plasma	6.2, 7.3
211Å	FeXIV	active-region corona	6.3
335Å	FeXVI	active-region corona	6.4
94Å	FeXVIII	flaring corona	6.8
131Å	FeVIII, FeXXI	transition region, flaring corona	5.6, 7.0

This paper focuses primarily on the analysis of data from the second camera that measures linear and circular polarization with a 135s cadence frame list [171]. From these filtergrams the vector magnetic field and other plasma parameters can be derived.

Table 2.2: The position and central wavelength of different AIA channels. This table is taken from [167].

Telescope	Position	Center Wavelength
1	Top	335Å
1	Bottom	131Å
2	Top	211Å
2	Bottom	193Å
3	Top	UV/Visible
3	Bottom	171Å
4	Top	304Å
4	Bottom	94Å

2.1.3 SDO/EVE

Extreme Ultraviolet Variability Experiment (EVE) is mainly focusing on the understanding of solar EUV irradiance, how the EUV spectral irradiance varies, try to forecast the EUV spectral variability to avoid the geospace disturbances. Because the solar EUV radiance is the primary source of disturbances at the Earths atmosphere. Detailed information can be found in paper by [172].

2.2 The SOLIS

SOLIS (Synoptic Long-term investigations of the Sun) is one of the recent advances in a ground-based optical instrumentation for solar observation, It has proved the usefulness of ground-based synoptic data for making newer discoveries, in conjunction with space based data, such as those from SDO. Ground based systems are attractive because of distributed costs over several observatories spread across nations. Such a situation permits uninterrupted solar monitoring, overcoming barriers that constrain centrally focused observatories, particularly space based missions.

Figure 2.5: The NSO's SOLIS telescope mounted atop the Kitt Peak Vacuum Telescope.

The Synoptic Optical Long-term Investigations of the Sun has been designed and built via the National Solar Observatory (NSO) to advance our understanding of long-term changes in solar activity. In a nutshell, SOLIS is composed of a single equatorial mount carrying three telescopes: the 50 cm Vector Spectromagnetograph (VSM), the 14 cm Full-Disk Patrol (FDP), and the 8 mm Integrated Sunlight Spectrometer (ISS), Figure (2.5).

The prototype system is located on top of the Kitt Peak Vacuum Telescope building (see Fig. 2.5; left). SOLIS instruments are designed to address three major questions: What causes the solar cycle? How is energy stored and released in the solar atmosphere? How do the solar radiative and non-radiative outputs vary in time?

2.2.1 Vector Spectromagnetograph (VSM)

VSM is a 50 cm primary mirror and a two-lens field corrector telescope in which the entrance of the telescope is protected by a thin (6 mm) fused silica window and the whole telescope is filled with helium to minimize the internal seeing. A fan system circulates the helium to minimize the temperature gradients inside the telescope. The image of the Sun is built on the entrance slit. The length of the slit covers 2048 arcseconds (angular diameter of the Sun varies between 1896 and 1962 arcseconds during the year).

The image of spectra is formed near the spectrograph slit, where the focal beam-splitter splits the image of the spectrograph slit into two equal parts each of 1024 arcseconds long. Light from each part is reimaged to a separate CCD camera of 1024×512 pixels in size. The polarizing beam-splitters are located in front of each camera. With these optical arrangements, one camera is taking data from one solar hemisphere and the other camera records images of spectra from the other hemisphere. Both cameras are taking data in two orthogonal polarization states.

A full disk magnetogram is constructed by scanning the solar image, which is achieved by moving the telescope in declination. It takes about 0.6 seconds to record one scan line in FeI 6301-6302Å region, and about 1.2 seconds for the CaII 8542Å line. In addition to full disk, VSM can take a series of area scans by scanning portion of solar disk in the declination (e.g.; the giant filament area in this study). Additional technical details on VSM can be found in [173] and at SOLIS website [2].

Generally, One can obtain the following data products from VSM:

1. photospheric full-disk vector-magnetograms using the FeI 6301.5 and 6302.5Å

---

[2] http://solis.nso.edu/VSMoverview.html

lines (field strength, azimuth, inclination, flux, Doppler velocity, continuum intensity)

2. chromospheric full-disk magnetograms using the CaII 8542Å line (line-of-sight magnetic flux, Doppler velocity, line core intensity)

3. full-disk HeI 10830Å line characteristics (equivalent width, continuum intensity, Doppler velocity, line depth, line asymmetry, Doppler width, Si line width, Si line depth, Si Doppler velocity)

4. photospheric full-disk longitudinal magnetograms using the FeI 6301.5 and 6302.5Å lines (line-of-sight magnetic flux).

2.2.2 The Integrated Sunlight Spectrometer (ISS)

The ISS is designed to obtain both high (R = 300,000) and moderate (R = 30,000) spectral resolution observations of the Sun as a star over a broad range of wavelengths of 3500-11000Å. The optical feed for the ISS consists of an 8 mm diameter lens located on the side of main mount of VSM. The lens builds the image of the Sun on the input face of the fiber optic assembly, which transmits light to a McPherson 2m Czerny-Turner double-pass spectrograph. The spectrograph is located in a temperature controlled room inside the telescope tower. The use of the fiber optic feed insures the complete integration of the sight in angular and spatial directions as required for the Sun as a star observations. The spectra are recorded using a back-illuminated 512×1024 CCD camera in the focal plane of the spectrograph. Further details on the observations and the data reduction pertaining to the ISS can be found in [174].

2.2.3 The Full Disk Patrol (FDP)

The FDP is a full-disk imager that uses tunable Lyot filters and a 2048×2048 CCD camera (about 1 arcseconds pixel size). It is designed to take observations with high temporal cadence (about ten seconds) in several selected spectral lines including H, CaIIK, HeI 10830Å, continuum (white light), and photospheric lines, as well as the capability of observing Doppler velocity maps. In June 2011, the FDP has been integrated to the SOLIS and is now going taking observations. The FDP will provide crucial imaging data for space-weather forecasting, to help understand triggering and evolution of solar filament, flares and coronal mass ejections, and it will also complement space-based X-ray and EUV observations.

2.3 Data Analysis Techniques

In this study, we consider a giant filament observed by SDO and SOLIS on February 10, 2015 and we mainly deal with the study of 3D magnetic field structure, an electric current density and magnetic energy of the filament.

Atmospheric Imaging Assembly (AIA) provides full-disk images with high spatial and temporal cadence (Section 2.1.1). By using the continuous AIA images we study the flows and dynamics of the prominences. The AIA data are freely accessible from the website [3]. Calibration of the AIA data is described in the paper by [169]. A detailed description the AIA data calibration is also available on the web [4]. The AIA data has three levels of Calibration: level 0, level 1.0 and level 1.5.

Level 0 - It contains the raw elementary data.

Level 1.0 - It contains the compressed FITS files and all files are corrected for bad

---

[3] http : //www.lmsal.com/get aia data/

[4] https : //www.lmsal.com/sdodocs/doc/dcur/S DOD0060.zip/zip/entry/

pixels, flat field and cosmic ray spikes (these are formed due to the collisions of high energy particles). All higher level data are constructed from level 1.0.

level 1.5 - After getting the level 1.0 data, it has to be converted into level 1.5 by using the SolarSoft routine -aia-prep.pro. All images are corrected for its different plate scale and roll angle.

Photospheric line-of-sight (LOS) and vector magnetograms are retrieved from filtergrams with a plate scale of 0.5 arc-second. From filter-grams averaged over about ten minutes, Stokes parameters are derived and inverted using the Milne-Eddington (ME) inversion algorithm of [175] (the filling factor is held at unity). Within automatically identified regions of strong magnetic fluxes [176], the focus of view (FOV) inversion data are from the second HMI vector data release (JSOC data series: hmi.B-720s). The 180-degree azimuthal ambiguity in the strong field region is resolved using the Minimum Energy Algorithm [162, 163, 177]. For the weak field region where noise dominates, we adopt a radial-acute angle method to resolve the azimuthal ambiguity.

The SOLIS/VSM can provide photospheric full-disk vector-magnetograms using the FeI 6301.5 and 6302.5Å lines (field strength, azimuth, inclination, flux, Doppler velocity, continuum intensity) and extrapolation to the lower corona helps to study solar filaments.

Quick-look (QL) vector magnetograms were created based on an algorithm by [149]. Beginning January 2012, QL vector magnetograms are created using weak-field approximation [178]. The algorithm uses the Milne-Eddington model of solar atmosphere, which assumes that the magnetic field is uniform (no gradients) through the layer of spectral line formation [179]. It also assumes symmetric line profiles, disregards magneto-optical effects (e.g., Faraday rotation), and does not distinguish the contributions of magnetic and non-magnetic components in spectral line profiles (i.e., magnetic filling factor is set to unity). A complete inversion of the spectral data is performed later using a technique developed by [180]. The ME inversion is only performed for pixels with spectral line profiles above the noise level. For pixels below the polarimetric noise threshold, the magnetic field parameters are set to zero.

From the measurements, the azimuths of transverse magnetic field can be determined with 180-degree ambiguity. This ambiguity is resolved using the non-potential field calculation (NPFC; see [181]). The NPFC method was selected on the basis of a comparative investigation of several methods for 180-degree ambiguity resolution [163]. Both QL and ME magnetograms can be used for potential and/or force-free field extrapolation. However, in strong fields inside sunspots, the QL field strengths may exhibit an erroneous decrease inside the sunspot umbra due to so-called magnetic saturation. For this study, we choose to use fully inverted ME magnetograms.

3

Magnetic Field Modeling

The magnetic fields observed in the solar photosphere extend out in to the corona, where they structure the plasma, store free magnetic energy and produce a wide variety of phenomena. While the distribution and strength of magnetic fields are routinely measured in the photosphere, the same is not true for the corona, where the plasma has very low density. To understand the nature of coronal magnetic fields, theoretical models that use the photospheric observations as a lower boundary condition are required. Therefore, one can use the photospheric 3D numerical magnetic field models to infer magnetic field structures of solar filaments in the lower corona. The spatial resolution of measurements has improved steadily, and models are able to incorporate some departures from the force-free field approximation. Several of these models are now capable of reproducing the observed sheared coronal magnetic features. In the following subsections, basic coronal magnetic field models such potential field, linear force-free field and nonlinear force-free field will be discussed independently though we only use the potential and non-linear force-free field models in this thesis.

3.1 Potential Field Source Surface (PFSS) Model

Potential field models are the most straightforward and therefore most commonly used technique for modeling the global coronal magnetic fields, require only the LOS photospheric magnetic field component as boundary condition. Current-free equilibria are mathematically simple and represent the lowest possible energy state of a coronal magnetic field. For computations on a global scale the potential-field source-surface (PFSS) models assumes that the electric currents in the corona do not significantly influence the global field structure and all field lines become radial at the source surface (at about 2.5 solar radii; see [182] for details). These models are popular because they are easy to compute and are capable of reproducing the basic coronal magnetic field structure.

Potential field models have led to an almost routine type reconstruction, used for observational purposes [183], but also for building initial conditions for dynamical MHD numerical simulations [184, 185]. This assumption has proven to be adequate for many quiescent, old active regions and even for the non-eruptive global coronal-heliospheric interface (e.g., [186–188]). That is the models give a first impression on the global coronal field structure which do not contain free energy and therefore cannot erupt.

In electromagnetic theory the current-free magnetic field is the state of minimum energy subjected to the given boundary condition. In other words, the variational problem for solenoidal vector field $\boldsymbol{B}$ is given as

$$W = \int_V \frac{\boldsymbol{B}^2}{8\pi} dV = stationary \tag{3.1}$$

where, B_n is the normal component of $\boldsymbol{B}$ and given on the boundary surface S. This leads to the Euler equation for variational problem which reduces to $\nabla \times \boldsymbol{B} = 0$

and it can be shown that the solution is unique and that it makes the functional W minimum [189].

Therefore, the potential field models are only used to estimate the lowest-energy state corresponding to an observed line-of-sight magnetic field. For region that can support flares, coronal mass ejection and filament eruptions (regions that contain strong electric currents) the model do not provide any estimate of energy.

The magnetic scalar potential Φ is uniquely determinable if Φ itself or if its normal derivative $\partial_n \Phi$ is specified on the boundaries and, therefore, one has to solve a Dirichlet or Neumann boundary value problem, respectively. As the line-of-sight component of the magnetic field near the solar disk center is essentially radial it can determine the distribution of magnetic sources which show a straight forward relation to the current-free field above the photosphere, the Laplace field can also be calculated far off disk center from the line-of-sight components. A solution is obtained by solving the Laplace equation for Φ with the normal magnetic field as a boundary condition and standard methods, using either Greens functions or Eigen function expansions.

The solution of this boundary-value problem in a standard form of harmonic expansion in terms of Eigen solutions of the Laplace equation written in a spherical coordinate system, (r, θ, ϕ) can be obtained by assuming a currentless $(J = 0)$ approximation that holds either throughout the space above the photospheric surface S_p, or between the photosphere and some spherical surface S_s (source surface). Then, the force-free equation reduces to $\nabla \times \boldsymbol{B} = 0$, and can be rewritten using scalar potential Φ as

$$\boldsymbol{B} = -\nabla \Phi \tag{3.2}$$

Substituting Eq. (3.2) into divergence-free equation, $\nabla \cdot \boldsymbol{B} = 0$, one can find Laplace equation for Φ as

$$\nabla^2\Phi = 0 \tag{3.3}$$

Using separation of variable in spherical (r, θ, ϕ) coordinates Eq. (3.3) has the solution [190]:

$$\Phi(r,\theta,\phi) = \sum_{l=0}^{\infty}\sum_{m=-l}^{l}\left[A_{lm}r^{l} + B_{lm}r^{-(l+1)}\right]Y_{lm}(\theta,\phi) \tag{3.4}$$

where Y_lm are Spherical Harmonics expressed through the associated Legendre polynomials, $P_l^m(cos\theta)$ by eqation

$$Y_{lm}(\theta,\phi) = \sqrt{\frac{2l+1(l+m)!}{4\pi(l+m)!}}P_l^m(cos\theta)e^{im\phi} \tag{3.5}$$

where, A_{lm} and B_{lm} are the Spherical Harmonics coefficients. An integrable function g(θ, ϕ) can be represented as

$$g(\theta,\phi) = \sum_{l=0}^{\infty}\sum_{m=-l}^{l} C_{lm}Y_{lm}(\theta,\phi) \tag{3.6}$$

with C_lm given by

$$C_{lm} = \int_0^{2\pi}\int_0^{\pi} Y_{lm}^*(\theta,\phi)g(\theta,\phi)sin\theta d\theta d\phi \tag{3.7}$$

and $Y_{lm} = (-1)^m Y_{l,-m}$. From the radial component of the vector magnetic field measured on the photosphere at $r = R_\odot$, we can prescribe Von Neumann boundary condition as $B_r(R_\odot, \theta, \phi) = \frac{\partial\Phi}{\partial r}$ and applying Eq. (3.7) to calculate C_{lm} for g$(\theta, \phi) = B_r(R_\odot, \theta, \phi)$. Hence the radial component of the magnetic field is given by

$$B_r(r,\theta,\phi) = \sum_{l=0}^{\infty}\sum_{m=-l}^{l}\left[A_{lm}lr^{l-1} + B_{lm}(l+1)r^{-(l+2)}\right]Y_{lm}(\theta,\phi) \tag{3.8}$$

The values of A_{lm} and B_{lm} are not completely determined with C_{lm} , hence we have to impose additional boundary condition with the assumption that magnetic field at source surface S_s is completely radial at $r \geq r_s$ as:

$$B_\theta = \frac{1}{r}\frac{\partial\Phi(r,\theta,\phi)}{\partial\theta} = 0 \quad \text{and} \quad B_\phi = \frac{1}{rsin\theta}\frac{\partial\Phi(r,\theta,\phi)}{\partial\phi} = 0 \quad \text{at} \quad r = r_s \tag{3.9}$$

Consequently the potential depends only on the radial component $r \geq r_s$, where

$$\Phi(r) = \sum_{l=0}^{\infty} \sum_{m=-l}^{l} \left[A_{lm} r^l + B_{lm} r^{-(l+1)} \right]$$

and all coefficient of Y_{lm} except $Y_{00} = 1$ have to vanish. Together with the photospheric boundary condition Eq. (3.7), one can get two equations to calculate A_{lm} and B_{lm} for $l \geq 1$:

$$A_{lm} l R_{\odot}^{l-1} - B_{lm}(l+1) R_{\odot}^{-(l+2)} = C_{lm} \tag{3.10}$$

$$A_{lm} r_s^l + B_{lm} r_s^{-(l+1)} = 0 \tag{3.11}$$

which leads to:

$$A_{lm} = \frac{C_{lm} R_{\odot}^{l+2}}{r_s^{2l+1} l (R_{\odot}^{l+2} + r_s^{2l+1})} \tag{3.12}$$

$$B_{lm} = -\frac{C_{lm} R_{\odot}^{l+2} r_s^{2l+1}}{r_s^{2l+1} l (R_{\odot}^{l+2} + r_s^{2l+1})} \tag{3.13}$$

The distance of the source surface sphere r_s might be chosen in a way that we can fit some additional constraints, e.g., observations of radiating loops or helmet streamer. We might compare the magnetic field and observed plasma structures similar as for the Cartesian linear force-free case and minimize with respect to r_s . Therefore, all components of potential field B can be calculated analytically from Φ.

In general, even if there are several limitations to potential field models which led to the introduction of the so-called constant-α and non-constant-α force-free hypothesis (both allow for the presence of electric currents in the corona), the potential field has been used as initial condition for many nonlinear force-free model codes for extrapolating coronal magnetic field.

3.2 Linear Force-free Fields

A generalized representation of linear-force field (LFFF) was first described by [191] to provide (non-unique) solutions of force-free equation using a Fourier series expansion in Cartesian coordinates. [192] used a Fourier representation to seek the solution to the set of linear force-free equations in a Cartesian coordinate system. He pointed out that fields being linear force-free in the whole volume outside the Sun neither possess a finite energy content nor can be determined uniquely from the normal photospheric magnetic field component alone. In other words, he found that the consideration of global-scale LFFF fields is problematic.

For special case that α has the same value (for LFFF), the variation in force-free problem lead to a linear differential equation and collapse to the potential field when α vanishes.

The proportionality constant α is the ratio of the vertical (LOS) current density and the vertical (LOS)magnetic field magnitude, and that the vertical (LOS) current density can be derived from the horizontal (transverse) magnetic field, where the knowledge of all three vector components of the magnetic field is required. Moreover, comparing model magnetic field lines and coronal observations, either directly with coronal loops seen in EUV images, or coronal loops extracted from such images, α can be deduced and/or optimized.

On global scales, although the LFFF are not frequently employed, they are mathematically and computationally possible, specially for two main reasons. Firstly, the maximum allowed value of α scales with the inverse of the length scale of the computational domain. Consequently very small values of α are possible but they are so small that they have no significant effect (i.e., the resulting magnetic field is almost similar to a potential field configurations). Secondly, observations show that both signs of α can be present in different regions on the Sun, at the same time. This is a contradiction to the LFFF assumption, namely that α is constant (i.e., has the same value for different regions on the Sun).

On smaller scales (i.e., to analyze active regions), however, LFFF models were used, though more frequently before the time when vector magnetograms started to became routinely available (as provided to date by, e.g., SDO/HMI). On these smaller scales, the maximum value of α can be significantly larger than on global scales and consequently active-region LFFF can be very different from potential ones, e.g., the associated field lines can be sheared. Also for LFFF models employed on active-region (AR) scales, however, the observation of different values of α in different portions of the same AR contradicts the basic assumption of a single value of α being representative for the entire AR under consideration.

3.3 Nonlinear Force-free Fields

Despite the popularity and frequent use of the simplified models (potential and linear force-free field), there are several limitations in these models. Both observational and theoretical arguments show that the magnetic field prior to eruptive processes in the corona is neither potential nor linear force-free field [193].

On the other hand, the non-linear force-free field (NLFFF) extrapolations for which α is a function of position shows the most realistic results [194]. It is a realistic way to model the non-potential coronal fields in active regions is to assume that the electric currents are parallel to the magnetic field, $\nabla \times \boldsymbol{B} = \alpha(r)\boldsymbol{B}$, with α being constant only along every field line ($\boldsymbol{B} \cdot \nabla\alpha = 0$), but varying from field line to field line, giving us the nonlinear force-free field (NLFFF).

NLFFF extrapolations require the three components of the magneticfield $(B_r, B_\theta, B_\phi$ for spherical geometry). A flux rope structure is obtained from NLFFF extrapolations of the magnetic field of an active region for the first time by [195]. Later, a few works have been presented in order to detect a flux rope topology sustaining a filament by using NLFFF extrapolations starting from the photosphere (e.g., [196–198]). However, [196] also found a sheared arcade structure in a different section of the same filament. Different methods for computing NLFF fields have been given by [193]. The corresponding numerical implementations have been intensively reviewed, and repeatedly evaluated and improved within the last decade (see [199–201]). The numerical schemes have been implemented in cartesian and spherical geometry to infer filaments magnetic field. As boundary condition, either the magnetic field vector at the bottom boundary of the computational domain or, alternatively, the vertical magnetic field and vertical electric current density is usually required. In this particular thesis, we use an optimization method where a global functional of $\boldsymbol{B}$ is minimized.

Due to low plasma-β in the corona, it is difficult to compute NLFFF though this does not work in the photosphere. In the photosphere, β is on average of the order of unity or more [202], although locally considerable smaller values may be found. The photospheric measurements as boundary condition for NLFFF computations has to be carefully considered. Because it cannot be guaranteed that the photospheric magnetic field vector is consistent with the assumption of a force-free field in the corona. It is possible to find out whether the vector magnetic field measurements are consistent by writing the force-free equations as the divergence of the Maxwell stress tensor, integration over the entire computational volume and applying Gauss' law. For force-free consistency, the value of the resulting surface integrals has to vanish, or in practice must then be sufficiently small. Theoretically, the surface integrals need to be evaluated over the entire boundary of the computational domain, but in practice this is only possible for the bottom (photospheric) boundary, where the field is measured.

Nonlinear force-free field extrapolation from vector magnetograms observed simultaneously at multiple heights (at a photospheric and chrmospheric level) has been performed by [203] to study the structure of an AR filament. One difficulty in combining and comparing two such data sets is that the exact height in the atmosphere of the chromospheric measurement is unknown. As a reasonable approximation, the authors assumed that the chromospheric measurements refer to the height of best agreement with the NLFFF reconstruction based on the photospheric vector field (about 2 Mm above the solar surface). Despite the difficulties discussed above, NLFFF extrapolations are a powerful tool for deriving the 3D coronal magnetic field above active regions and solar filaments.

In order to use the force-free models, the measurement errors and non-magnetic forces in photospheric field which make the data inconsistent must be resolved. To deal with these uncertainties, one has to:

1. preprocess the surface measurements in order to make them compatible with a force-free field, and

2. keep a balance between the force-free constraint and deviation from the photospheric field measurements. Both methods contain free parameters, which have to be optimized for use with data (from SDO/HMI and SOLIS/VSM in this thesis). It has been already mentioned that the magnetic field is not force-free in either the photosphere or the lower chromosphere (with the possible exception of sunspot areas, where the field is exceptionally strong). Furthermore, measurement errors,

in particular for the transverse field components (e.g., perpendicular to the line of sight of the observer), will destroy the compatibility of a magnetogram with the condition of being force-free. One way to ease these problems is to preprocess the magnetograph data as suggested by [204]. The vector components of the total magnetic force and the total magnetic torque on the volume considered are given by six boundary integrals that must vanish if the magnetic field is force-free in the full volume [205–207]. The preprocessing changes the boundary values of B within the error margins of the measurement in such a way that the moduli of the six boundary integrals are minimized. The resulting boundary values are expected to be more suitable for an extrapolation into a force-free field than the original values.

3.3.1 Preprocessing Procedure in Spherical Geometry

We know that the magnetic field is not force-free in either the photosphere or the lower chromosphere (with the possible exception of sunspot areas, where the field is exceptionally strong). Furthermore, measurement errors, in particular for the transverse field components (eg. perpendicular to the line of sight of the observer), will destroy the compatibility of a magnetogram with the condition of being force-free. However, the problems are solved by using preprocessing procedure of the magnetogram data.

The vector components of the total magnetic force and the total magnetic torque on the volume considered are given by six boundary integrals that must vanish if the magnetic field is force-free in the full volume.

In this work, we use a spherical version of both the preprocessing and the optimization code for restricted parts of the Sun, large area which accommodates the giant solar filament. A preprocessing routine in spherical geometry is used to deal with noisy data and data with other uncertainties. While preprocessing does not model the details of the interface between the forced photosphere and the force-free base of the solar corona the procedure helps us to find suitable boundary conditions for a force-free modelling from measurements with inconsistencies.

Boundary Conditions in Spherical Geometry

The force-free and torque-free conditions for spherical geometry can be formulated as in [208], and the integrated forms of the equation for the free-force magnetic fields were summarized [209]. The Lorentz force is

$$\boldsymbol{F} = \frac{1}{4\pi}(\nabla \times \boldsymbol{B}) \times \boldsymbol{B} \tag{3.14}$$

where B is the magnetic field vector. By integrating Eq. (3.14) over a volume V surrounded by a surface S one can obtain a global force-balance equation.

$$\int_V \boldsymbol{F} dV = \int_V (\nabla \times \boldsymbol{B}) \times \boldsymbol{B} dV = 0 \tag{3.15}$$

But, imploying the vector identity:

$$\nabla(\boldsymbol{A} \cdot \boldsymbol{B}) = \boldsymbol{A} \times (\nabla \times \boldsymbol{B}) + \boldsymbol{B} \times (\nabla \times \boldsymbol{A}) + (\boldsymbol{A} \cdot \nabla)\boldsymbol{B} + (\boldsymbol{B} \cdot \nabla)\boldsymbol{A} \tag{3.16}$$

If $\boldsymbol{A} = \boldsymbol{B}$, the identity reduces to

$$(\nabla \times \boldsymbol{B}) \times \boldsymbol{B} = -\nabla(\frac{1}{2}\boldsymbol{B}^2) + (\boldsymbol{B} \cdot \nabla)\boldsymbol{B} \tag{3.17}$$

from HMI data substituting equation (3.17) into equation (3.15) and using Gauss divergence theorem one can find,

$$\frac{1}{2}\int_S \boldsymbol{B}^2 d\boldsymbol{S} - \int_S (\boldsymbol{B} \cdot d\boldsymbol{S})\boldsymbol{B} = 0 \tag{3.18}$$

The vector $d\boldsymbol{S}$ is directed into the volume V. We will consider the equation described above in spherical polar coordinates (r, θ, ϕ), with usual axes. The volume

V is space outside of a sphere of radius $R_\odot$ and the origin of the vector $\boldsymbol{r}$ is at the center of the sphere (Sun), with $d\boldsymbol{S} = ds\hat{\boldsymbol{e}}_r$ and $ds = R_\odot sin\theta d\theta d\phi$. The force balance equation (3.18) is still valid if S is spherical surface. For magnetic field vector,

$$\boldsymbol{B} = B_r\hat{\boldsymbol{e}}_r + B_\theta\hat{\boldsymbol{e}}_\theta + B_\phi\hat{\boldsymbol{e}}_\phi$$

with

$$\boldsymbol{B} \cdot d\boldsymbol{S} = B_r ds$$

equation (3.18) becomes

$$\int_S \frac{1}{2}(B_r^2 + B_\theta^2 + B_\phi^2)d\boldsymbol{S} - \int_S B_r ds(B_r\hat{\boldsymbol{e}}_r + B_\theta\hat{\boldsymbol{e}}_\theta + B_\phi\hat{\boldsymbol{e}}_\phi) = 0 \qquad (3.19)$$

Notice that the spherical unit vectors vary over S . For the numerical evaluation, we therefore calculate the cartesian components of Eq. (3.19). One can derive the force and torque balance equations for the three components as follows:

For force-balance condition along x-axis, we have

$$\int_{r>R_\odot} F_x dV = 0$$

Multiplying equation (3.19) by $\hat{\boldsymbol{e}}_x$

$$\hat{\boldsymbol{e}}_x \cdot \left[\int_S \frac{1}{2}(B_r^2 + B_\theta^2 + B_\phi^2)d\boldsymbol{S} - \int_S B_r ds(B_r\hat{\boldsymbol{e}}_r + B_\theta\hat{\boldsymbol{e}}_\theta + B_\phi\hat{\boldsymbol{e}}_\phi)\right] = 0 \qquad (3.20)$$

Using the spherical unit vectors

$$\hat{\boldsymbol{e}}_r = sin\theta cos\phi\hat{\boldsymbol{e}}_x + sin\theta sin\phi\hat{\boldsymbol{e}}_y + cos\theta\hat{\boldsymbol{e}}_z$$

$$\hat{\boldsymbol{e}}_\theta = cos\theta cos\phi\hat{\boldsymbol{e}}_x + cos\theta sin\phi\hat{\boldsymbol{e}}_y - sin\theta\hat{\boldsymbol{e}}_z$$

$$\hat{\boldsymbol{e}}_\phi = -sin\phi\hat{\boldsymbol{e}}_x + cos\phi\hat{\boldsymbol{e}}_y$$

hence,

$$\hat{\boldsymbol{e}}_x \cdot \hat{\boldsymbol{e}}_r = sin\theta cos\phi$$

$$\hat{\boldsymbol{e}}_x \cdot \hat{\boldsymbol{e}}_\theta = cos\theta cos\phi$$

$$\hat{\boldsymbol{e}}_x \cdot \hat{\boldsymbol{e}}_\phi = -sin\phi$$

Using those conditions one can arrive at

$$\int_S \left[\frac{1}{2}(B_\theta^2 + B_\phi^2 - B_r^2)sin\theta cos\phi - B_r B_\theta cos\theta cos\phi + B_r B_\phi sin\phi\right] d\Omega = 0 \tag{3.21}$$

Similarly for force-balance condition along y-component is

$$\int_{r>R_\odot} F_y dV = 0$$

$$\hat{\boldsymbol{e}}_y \cdot \left[\int_S \frac{1}{2}(B_r^2 + B_\theta^2 + B_\phi^2) d\boldsymbol{S} - \int_S B_r ds(B_r \hat{\boldsymbol{e}}_r + B_\theta \hat{\boldsymbol{e}}_\theta + B_\phi \hat{\boldsymbol{e}}_\phi)\right] = 0$$

This leads to

$$\int_S \left[\frac{1}{2}(B_\theta^2 + B_\phi^2 - B_r^2)sin\theta sin\phi - B_r B_\theta cos\theta sin\phi - B_r B_\phi cos\phi\right] d\Omega = 0 \tag{3.22}$$

The force-balance along the z-component is

$$\int_{r>R_\odot} F_z dV = 0$$

$$\hat{\boldsymbol{e}}_z \cdot \left[\int_S \frac{1}{2}(B_r^2 + B_\theta^2 + B_\phi^2) d\boldsymbol{S} - \int_S B_r ds(B_r \hat{\boldsymbol{e}}_r + B_\theta \hat{\boldsymbol{e}}_\theta + B_\phi \hat{\boldsymbol{e}}_\phi)\right] = 0$$

Then

$$\int_S \left[\frac{1}{2}(B_\theta^2 + B_\phi^2 - B_r^2)cos\theta + B_r B_\theta sin\theta\right] d\Omega = 0 \tag{3.23}$$

For the torque balance equations, the volume integral of torque in the box, in the field of view, must vanish.

$$\int_V (\boldsymbol{r} \times \boldsymbol{F}) dV = 0$$

Using Gauss divergence theorem this will reduce to

$$\int_V (\boldsymbol{r} \times \boldsymbol{F}) dV = \frac{1}{2}\int_S B^2(\boldsymbol{r} \times d\boldsymbol{S}) - \int_S (\boldsymbol{r} \times \boldsymbol{B})(\boldsymbol{B} \cdot d\boldsymbol{S}) = 0$$

Using $\boldsymbol{r} = R_{\odot}\hat{\boldsymbol{e}}_r$, $(\boldsymbol{r} \times d\boldsymbol{S}) = 0$ and $\boldsymbol{B} \cdot d\boldsymbol{S} = B_r d\Omega$

The above equation reduces to

$$\int_S (\boldsymbol{r} \times \boldsymbol{B}) B_r d\Omega = 0 \tag{3.24}$$

Using the cross product

$$\boldsymbol{r} \times \boldsymbol{B} = 0\hat{\boldsymbol{e}}_r - R_{\odot}B_{\phi}\hat{\boldsymbol{e}}_{\theta} + R_{\odot}B_{\theta}\hat{\boldsymbol{e}}_{\phi}$$

Then equation (3.24) becomes

$$\int_S \left[-R_{\odot}B_{\phi}\hat{\boldsymbol{e}}_{\theta} + R_{\odot}B_{\theta}\hat{\boldsymbol{e}}_{\phi}\right] B_r d\Omega = 0 \tag{3.25}$$

Hence the torque balance along each component will be

$$\hat{\boldsymbol{e}}_x \cdot \left[\int_S (-R_{\odot}B_{\phi}\hat{\boldsymbol{e}}_{\theta} + R_{\odot}B_{\theta}\hat{\boldsymbol{e}}_{\phi}) B_r d\Omega\right] = 0$$

Which is actually reducing to

$$\int_S B_r (B_{\phi} cos\theta cos\phi + B_{\theta} sin\phi) d\Omega = 0 \tag{3.26}$$

Similarly

$$\hat{\boldsymbol{e}}_y \cdot \left[\int_S (-R_{\odot}B_{\phi}\hat{\boldsymbol{e}}_{\theta} + R_{\odot}B_{\theta}\hat{\boldsymbol{e}}_{\phi}) B_r d\Omega\right] = 0$$

Then

$$\int_S B_r (B_{\phi} cos\theta sin\phi - B_{\theta} cos\phi) d\Omega = 0 \tag{3.27}$$

Finally

$$\hat{\boldsymbol{e}}_z \cdot \left[\int_S (-R_{\odot}B_{\phi}\hat{\boldsymbol{e}}_{\theta} + R_{\odot}B_{\theta}\hat{\boldsymbol{e}}_{\phi}) B_r d\Omega\right] = 0$$

hence

$$\int_S B_r B_{\phi} sin\theta d\Omega = 0 \tag{3.28}$$

1. The total force on the boundary has to vanish because force-free fields can not exert pressure on the photospheric boundary S and cannot induce shear stresses

along axes parallel to the boundaries, i.e.,

$$F_1 = \int_S \left[\frac{1}{2}(B_\theta^2 + B_\phi^2 - B_r^2) sin\theta cos\phi - B_r B_\theta cos\theta cos\phi + B_r B_\phi sin\phi \right] d\Omega = 0 \tag{3.29}$$

$$F_2 = \int_S \left[\frac{1}{2}(B_\theta^2 + B_\phi^2 - B_r^2) sin\theta cos\phi - B_r B_\theta cos\theta cos\phi - B_r B_\phi sin\phi \right] d\Omega = 0 \tag{3.30}$$

$$F_3 = \int_S \left[\frac{1}{2}(B_\theta^2 + B_\phi^2 - B_r^2) cos\theta + B_r B_\theta sin\theta \right] d\Omega = 0 \tag{3.31}$$

2. The total torque on the boundary vanishes or force-free fields cannot induce rotational moments along the boundary

$$\tau_1 = \int_S B_r (B_\phi cos\theta cos\phi + B_\theta sin\phi) d\Omega = 0 \tag{3.32}$$

$$\tau_2 = \int_S B_r (B_\phi cos\theta sin\phi - B_\theta cos\phi) d\Omega = 0 \tag{3.33}$$

$$\tau_3 = \int_S B_r B_\phi sin\theta d\Omega = 0 \tag{3.34}$$

The relations given in Eqs.(3.29–3.34) are always fulfilled for potential magnetic fields because of the vanishing electric currents ($\mathbf{J} = 0$). However, if currents flow on either side of S, both impulse and momentum can be transferred from one side to the other and the distribution of the field in the plane may not satisfy these relations.

As with the flux balance these criteria must in general be applied to the entire surface of the numerical box. Since we assumed that the photospheric flux is sufficiently concentrated in the center and the net flux is in balance, we can expect the magnetic field on the lateral and top boundaries to remain weak and hence these surfaces do not represent a significant contribution to the integrals of the constraints above. We therefore impose the criteria on the bottom boundary alone.

1. The flux balance parametres

$$\epsilon_{flux} = \frac{\int_S B_r d\Omega}{\int_S |B_r| d\Omega} \tag{3.35}$$

2. force balance parameter is

$$\epsilon_{force} = \frac{|F_1| + |F_2| + |F_3|}{E_B} \tag{3.36}$$

$$\epsilon_{force} = \Big(|\int_S [E_B^- sin\theta cos\phi - B_r B_1] d\Omega| + |\int_S [E_B^- sin\theta sin\phi - B_r B_2] d\Omega| \\ + |\int_S [E_B^- sin\theta cos\phi - B_r B_\theta sin\theta] d\Omega| \Big) / E_B \tag{3.37}$$

3. The torque balance parameter is

$$\epsilon_{torque} = \frac{|\tau_1| + |\tau_2| + |\tau_3|}{E_B} \tag{3.38}$$

$$\epsilon_{torque} = \Big(|\int_S B_r B_3 d\Omega| + |\int_S B_r B_4 d\Omega| + |\int_S B_r B_\phi sin\theta d\Omega| \Big) / E_B \tag{3.39}$$

Where the following notation is used for simplicity:

$$E_B^- = \frac{1}{2}(B_\theta^2 + B_\phi^2 - B_r^2), \;\; E_B = \int_S (B_r^2 + B_\theta^2 + B_\phi^2) d\Omega$$

$$B_1 = B_\theta cos\theta cos\phi - B_\phi sin\phi, \;\; B_2 = B_\theta cos\theta sin\phi + B_\phi cos\phi$$

$$B_3 = B_\phi cos\theta cos\phi + B_\theta sin\phi, \;\; B_4 = B_\phi cos\theta sin\phi - B_\theta cos\phi$$

An observed vector magnetogram is then flux-balanced and consistent with the force-free assumption if: $\epsilon_{flux} \ll 1$, $\epsilon_{force} \ll 1$ and $\epsilon_{torque} \ll 1$.

Numerical Methods of Preprocessing

To serve as suitable lower boundary condition for a force-free modeling, vector magnetograms have to be approximately flux balanced and on average a net tangential force acting on the boundary and shear stresses along axes lying on the boundary have to reduce to zero. We use dimensionless parameters, ϵ_{flux}, ϵ_{force}, and ϵ_{torque} to quantify such properties [121, 204, 205]. Even if we choose a sufficiently flux balanced region (ϵ_{flux}), we find that the force-free conditions $\epsilon_{force} \ll 1$

and $\epsilon_{torque} \ll 1$ are not usually fulfilled for measured vector magnetograms. Therefore, force-free extrapolation methods should not be used directly on observed vector magnetograms which usually have noisy transverse photospheric magnetic field measurements. The large noise in the transverse components of the photospheric field vector, which is one order of magnitude higher than on the LOS-field (the transverse B_θ and B_ϕ at the bottom boundary), provides us freedom to adjust these data within the noise level. In order to fulfill those conditions, we use the preprocessing scheme of [121] that minimizes a two-dimensional functional of quadratic form in spherical geometry which was implemented in [204] for Cartesian coordinate system.

$$\boldsymbol{B} = argmin(L) \tag{3.40}$$

$$L = \mu_1 L_1 + \mu_2 L_2 + \mu_3 L_3 + \mu_4 L_4 \tag{3.41}$$

where $\boldsymbol{B}$ is the preprocessed surface magnetic field from the input observed field, $\boldsymbol{B}_{obs}$. Each of the constraints L_n is weighted by as yet undetermined factor μ_n . The first term $(n = 1)$ corresponds to the force-balance condition, the next $(n = 2)$ to the torque-free condition, and the last term $(n = 4)$ controls the smoothing. The term $(n = 3)$ controls the difference between measured and preprocessed vector fields. The explicit form of L_1, L_2, L_3 and L_4 in spherical coordinate system can be written as:

$$L_1 = F_1 + F_2 + F_3 \tag{3.42}$$

$$\begin{aligned} L_1 = &\left(\sum_p [E_B^- sin\theta cos\phi - B_r B_1] sin\theta\right)^2 \\ &+\left([E_B^- sin\theta sin\phi - B_r B_2] sin\theta\right)^2 \\ &+\left(E_B^- sin\theta cos\phi - B_r B_\theta sin\theta] sin\theta\right)^2 \end{aligned} \tag{3.43}$$

$$L_2 = \tau_1 + \tau_2 + \tau_3 \tag{3.44}$$

$$L_2 = \left(\sum_p B_r B_3 sin\theta\right)^2 + \left(\sum_p B_r B_4 sin\theta\right)^2 + \left(\sum_p B_r B_\phi sin^2\theta\right)^2 \tag{3.45}$$

$$L_3 = \sum_p \left[(B_r - B_{robs})^2 + (B_\theta - B_{\theta obs})^2 + (B_\phi - B_{\phi obs})^2\right] \tag{3.46}$$

$$L_4 = \sum_p \left[(\Delta B_r)^2 + \Delta B_\theta)^2 + \Delta B_\phi)^2\right] \tag{3.47}$$

The surface integrals are replaced by a summation ($\int_S d\Omega \rightarrow \sum_p sin\theta\Delta\theta\Delta\phi$, omitting the constant $\Delta\theta\Delta\phi$ over all p grid nodes of the bottom surface grid, with an elementary surface of $sin\theta\Delta\phi \times \Delta\theta$). The differentiation in the smoothing term (L_4) is achieved by the usual five-point stencil for the 2D-Laplace operator.

The derivative of L with respect to each of the three field components at every node (q) of the bottom boundary grid must be obtained in order to get Eq. (3.40) by iteration [124]. We have, however, taken into account that B_r is measured with much higher accuracy than B_θ and B_ϕ . This is achieved by assuming that the vertical component is invariable compared to horizontal components in all terms where mixed products of the vertical and horizontal field components occur, e.g., within the constraints [204]. The relevant functional derivatives of L are therefore:

$$\frac{\partial L}{\partial (B_r)q} = 2\mu_3(B_r - B_{robs})_q + 2\mu_4(\Delta(\Delta B_r))_q \tag{3.48}$$

$$\begin{aligned} \frac{\partial L}{\partial (B_\theta)q} = {} & 2\mu_1(B_\theta sin^2\theta cos\phi - B_r sin\theta cos\theta cos\phi)_q \times \\ & \sum_p [E_B^- sin\theta cos\phi - B_r B_1] sin\theta \\ & +2\mu_1(B_\theta sin^2\theta sin\phi - B_r sin\theta cos\theta sin\phi)_q \times \\ & \sum_p [E_B^- sin\theta sin\phi - B_r B_2] sin\theta \\ & +2\mu_1(B_\theta sin\theta cos\theta + B_r sin^2\theta)_q \times \\ & \sum_p [E_B^- cos\theta + B_r B_\theta] sin\theta \end{aligned} \tag{3.49}$$

$$
\begin{aligned}
&+2\mu_2\Bigg[(B_r sin\theta sin\phi)_q \sum_p B_r B_3 sin\theta \\
&-(B_r sin\theta cos\phi)_q \sum_p B_r B_4 sin\theta\Bigg] \\
&+2\mu_3(B_\theta - B_{\theta obs})_q + 2\mu_4(\Delta(\Delta B_\theta))_q
\end{aligned}
$$

$$
\begin{aligned}
\frac{\partial L}{\partial(B_\phi)q} &= 2\mu_1(B_\phi sin^2\theta cos\phi + B_r sin\theta sin\phi)_q \times \\
&\sum_p [E_B^- sin\theta cos\phi - B_r B_1] sin\theta \\
&+2\mu_1(B_\phi sin^2\theta sin\phi - B_r sin\theta cos\phi)_q \times \\
&\sum_p [E_B^- sin\theta sin\phi - B_r B_2] sin\theta \qquad (3.50) \\
&+2\mu_1(B_\phi sin\theta cos\theta)_q \times \\
&\sum_p [E_B^- cos\theta + B_r B_\theta sin\theta] sin\theta \\
&+2\mu_2\Bigg[(B_r cos\theta cos\phi sin\theta)_q \sum_p B_r B_3 sin\theta \\
&+(B_r cos\theta sin\phi sin\theta)_q \sum_p B_r B_4 sin\theta \\
&+(B_r sin^2\theta)_q \sum_p B_r B_\phi sin^2\theta\Bigg] + 2\mu_3(B_\phi - B_{\phi obs})_q \\
&+2\mu_4(\Delta(\Delta B_\phi))_q
\end{aligned}
$$

The optimization is performed iteratively by using Landweber iteration.[1]

3.3.2 Optimization Procedure

The optimization procedure is one of several methods that have been developed over the past few decades to compute the most general class of those force-free fields. Solving the force-free magnetic fields Equations (1.1) and (1.3) with the help of an optimization principle as proposed by [210] for the calculation of nonlinear

---

[1] Landweber iteration is the method used for finding successively better approximations to the zeroes (or roots) of a real-valued function.

force-free fields using all six boundaries of a computational box, and later by [211] who has improved the method and showed that it is essentially equivalent to introducing finite size boundary regions on those boundaries where $\boldsymbol{B}$ is unknown with the weighting function $w(x, y, z)$ different from unity for Cartesian geometry. The weighting function is desirable to move these faces as far away as possible from the region of interest. The method minimizes a joint measure (L_ω) of the normalized Lorentz forces and the divergence of the field in the volume. Throughout this minimization, the photospheric boundary of the model field $\boldsymbol{B}$ is matched exactly to the observed $\boldsymbol{B}_{obs}$ and possibly preprocessed magnetogram values $\boldsymbol{B}$.

Here, we use the optimization approach for functional L_ω in spherical geometry [121, 212] along with the new method, which instead of an exact match enforces a minimal deviation between the photospheric boundary of the model field $\boldsymbol{B}$ and the magnetogram field $\boldsymbol{B}_{obs}$ by adding an appropriate surface integral term L_{photo} [124, 213]. These terms are given by

$$\boldsymbol{B} = argmin(L_\omega)$$

$$L_\omega = L_f + L_d + \nu L_{photo} \tag{3.51}$$

$$L_f = \int_V \omega_f(r,\theta,\phi) B^{-2} |(\nabla \times \boldsymbol{B}) \times \boldsymbol{B}|^2 r^2 sin\theta dr d\theta d\phi$$

$$L_d = \int_V \omega_d(r,\theta,\phi) |(\nabla \cdot \boldsymbol{B})|^2 r^2 sin\theta dr d\theta d\phi$$

$$L_{photo} = \int_S (\boldsymbol{B} - \boldsymbol{B}_{obs}) \cdot \boldsymbol{W}(\theta,\phi) \cdot (\boldsymbol{B} - \boldsymbol{B}_{obs}) r^2 sin\theta d\theta d\phi$$

where L_f and L_d measure how well the force-free Eq. (1.1) and divergence-free Eq. (1.3) conditions are fulfilled, respectively, and both $\omega_f(r, \theta, \phi)$ and $\omega_d(r, \theta, \phi)$ are weighting functions. The weighting functions ω_f and ω_d in L_f and L_d in Eq. (3.51) are chosen to be unity within the inner physical domain V' and decline with a cosine profile in the buffer boundary region [121]. They reach a zero value at the boundary of the outer volume V. The third integral, L_{photo}, is the surface integral over the photosphere which allows us to relax the field on the photosphere towards force-free solution without too much deviation from the original surface field data.

$\mathbf{W}(\theta, \phi)$ is a space-dependent diagonal matrix the element of which are inversily proportional to the estimated squared measurement error of the respective field component. In principle one could compute **W** from the measurement noise and errors obtained from the inversion of measured Stokes profiles to field components. Until these quantities become available, a reasonable assumption is that the magnetic field is measured in strong field regions more accurately than in the weak field and that the error in the photospheric transverse field is at least one order of magnitude higher as the line-of-sight component. Appropriate choices to optimize ν and **W** for use with SDO/HMI [214] and SOLIS/VSM [124] magnetograms have been investigated.

4

Results and Discussion

The main purpose of this work is to study magnetic field, an electric current density, free energy of the giant filament observed on February 10, 2015 (see Fig. 4.1) via SDO/HMI and SOLIS/VSM instruments using the PFSS and NLFFF models in spherical coordinates. Topological magnetic field lines of the filament have been plotted both from PFSS and NLFFF models to see which model is more adequate for the study.

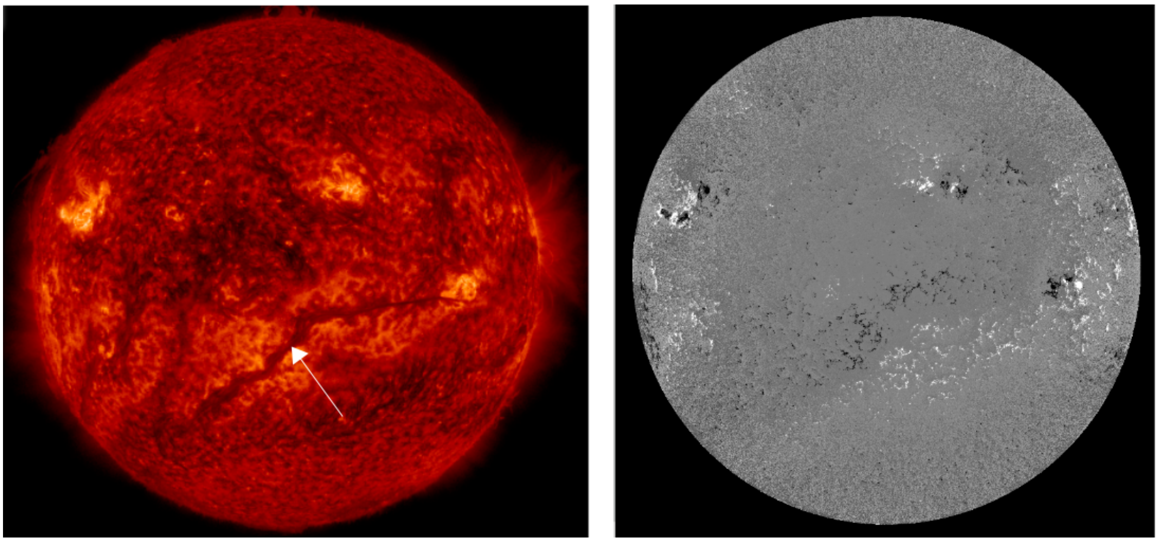

Figure 4.1: The giant filament observed by SDO/AIA at 304Å is shown using arrow on the left hand side while the corresponding SDO/HMI magnetogram is shown on the right.

The giant filament with length over 800 Mm (see Fig. 4.1) was observed during

Carrington (CR) 2160 (from February 2, 2015 to February 28, 2015). The SDO/HMI daily synoptic map and SOLIS/VSM near real time synoptic map during the period is shown in Figures (4.2) and (4.3), respectively, where the horizontal line is the latitude and the vertical line shows the Carrington longitude. The region of the filament has been shown by the rectangular solid line both for SDO/HMI and SOLIS/VSM magnetograms. The black and white spots on the surface indicate ARs, strongest magnetic field areas with different polarities. The maps show the magnitude of the radial component of the magnetic field during the Carrington rotation. During the period of CR2160, the only giant filament seen in the solar atmosphere was the one under this study and it is the biggest filament ever studded using PFSS and NLFFF models.

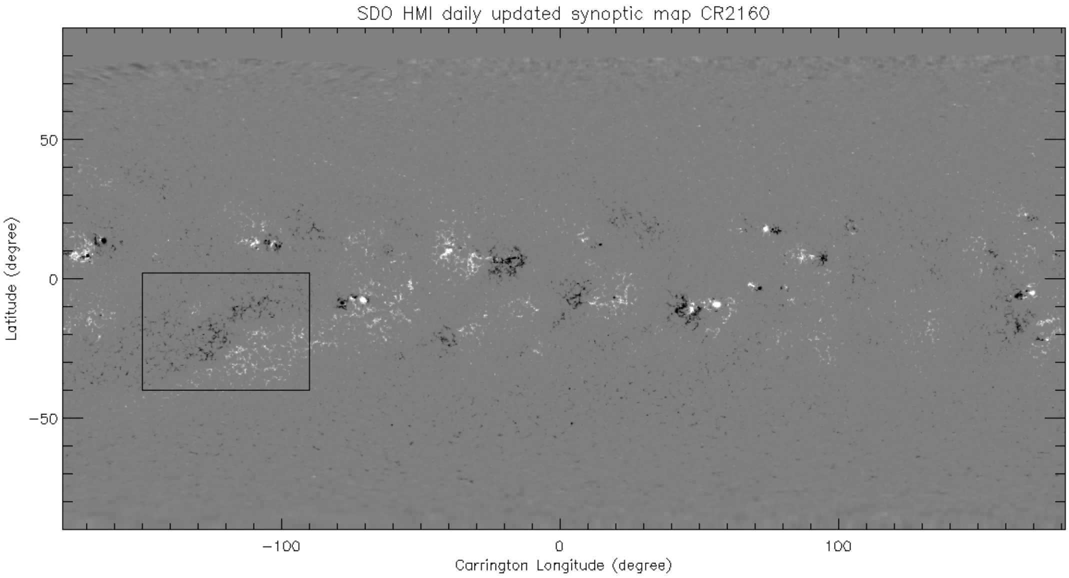

Figure 4.2: SDO/HMI daily updated synoptic map for CR2160 and the rectangular solid line indicates the filament region.

The cutout region from the daily updated synoptic maps is shown in Figures (4.4) and (4.5). The black and white regions are negative and positive polarities, respectively. We use spherical optimization solar soft (SSWIDL) code for a large

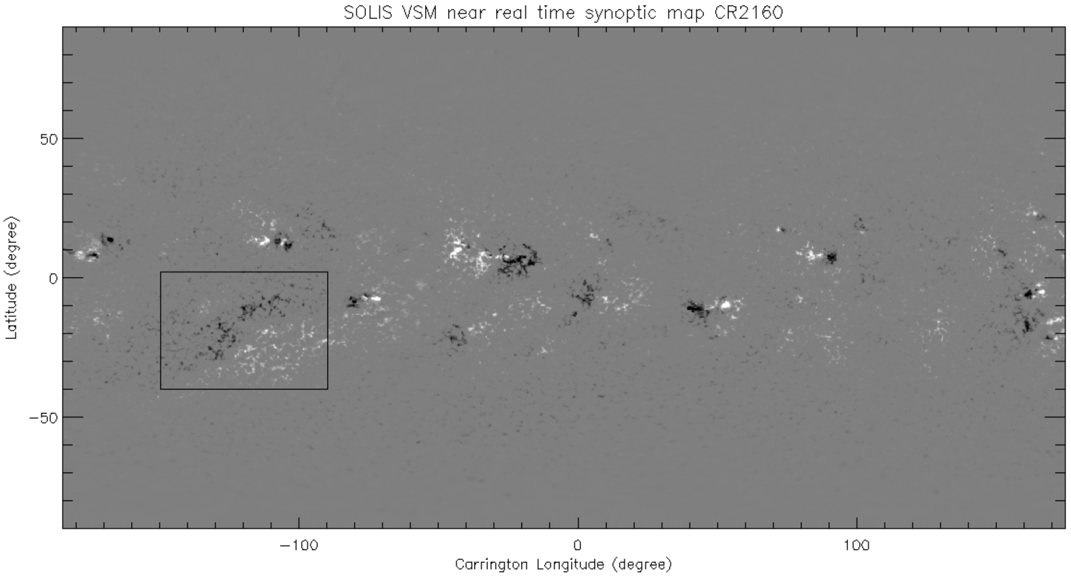

Figure 4.3: SOLIS/VSM near real time synoptic map for CR2160 and the rectangular solid line indicates the filament region.

region of corona where the filament is suspended, we adopt a uniform spherical grid using r, θ and ϕ with $n_r = 500$, $n_\theta = 350$, $n_\phi = 117$ grid points in the direction of radius, latitude and longitude, respectively, with the field of view of latitudes = [-40, 2] and longitudes = [-25, 35] on the spherical globe, which is enough to include almost all the length of the filament except the two ends.

Since the vector magnetogram data is not consistent with the force-free assumption, we use a preprocessing routine in spherical geometry, which derives suitable boundary conditions for force-free modeling from the measured photospheric data. Applying this procedure to both SDO/HMI and SOLIS/VSM reduces ϵ_{force} and ϵ_{torque} further significantly. The two quantities are very well below unity (e.g.: $\epsilon_{force} = 2.50 \times 10^{-6}$ and $\epsilon_{torque} = 2.31 \times 10^{-6}$ for SDO/HMI) after preprocessing, these indicate that the data can serve as suitable boundary condition for a force-free modeling. Doing these we approximate the magnetic field at a lower corona where magnetic forces are expected to dominate the other forces.

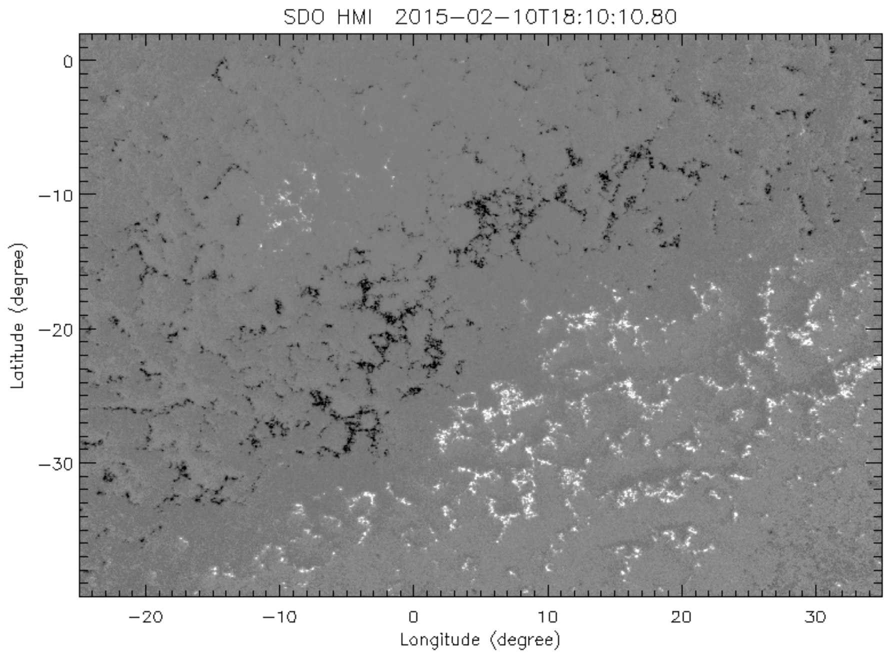

Figure 4.4: Cut-out region (FOV) from SDO/HMI daily updated synoptic map for CR2160.

A standard preprocessing parameters from HMI data are found: $\mu_1 = 0.1$ controls force freeness and $\mu_2 = 0.1$ controls torque freeness. We also obtain the optimal value for smoothing parameter $\mu_4 = 0.001$ and $\mu_3 = 0.0001$ controls the difference between measured and preprocessed vector fields for the filament region.

Table 4.1. Constraint for preprocessing $L_{12} = L_1 = L_2$, L_3, L_4 with their corresponding values before and after preprocessing for HMI data. The first column indicates iteration for preprocessing, in the first row 0 indicates no iteration which means observed values and in the second row 5000 iteration for preprocessing.

it	dL	L_{12}	L_3	L_4	L
0	1	5.16×10^{-2}	0	3.98×10^{-5}	5.16×10^{-3}
5000	2.9×10^{-3}	7.51×10^{-12}	3×10^{-7}	3.06×10^{-5}	3.06×10^{-8}

The preprocessing influences the structure of the magnetic vector data. It does not only smooth B_t (transverse field) but also alters its values in order to reduce the

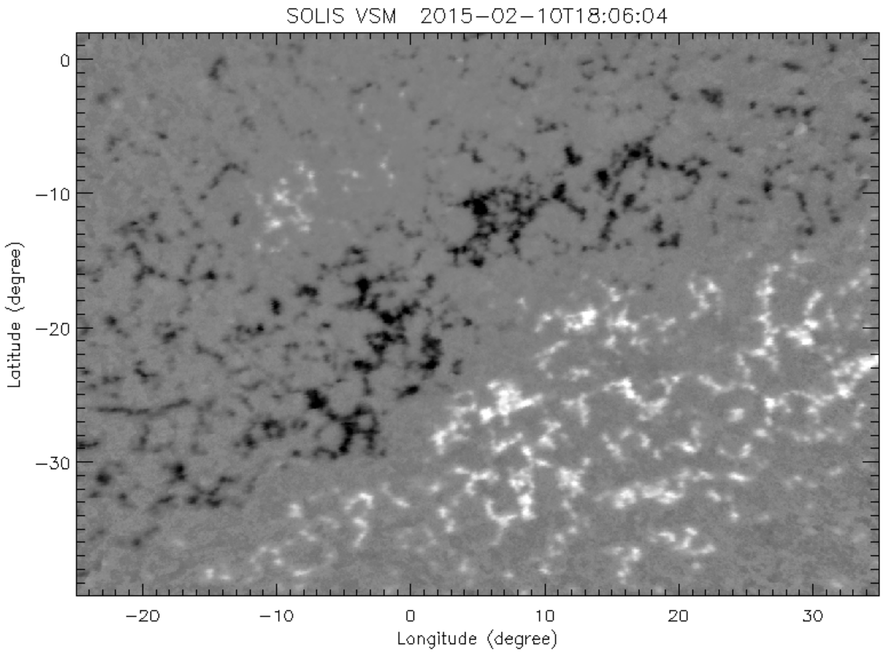

Figure 4.5: Cut-out region (FOV) from SOLIS/VSM near real time synoptic map for CR2160.

net force and torque. The change in B_t is more pronounced than the radial component B_r (radial field) since B_t is measured with lower accuracy than the longitudinal magnetic field. In Figures (4.6) and (4.7) the arrows show the horizontal components and the background indicates the radial component of the vector magnetic field after preprocessing for the FOV of SDO/HMI and SOLIS/VSM magnetograms, respectively.

In order to compute the potential field, we use the preprocessed radial component B_r of the HMI and VSM data using a spherical harmonic expansion. We implement NLFFF code initialized by the potential field solution (except for the observed bottom boundary) during relaxation towards a force-free state in the computational volume.

The field lines of the PFSS and NLFFF models are reconstructed from the same footpoints. The potential field lines observed in Fig. (4.8) are obtained from the

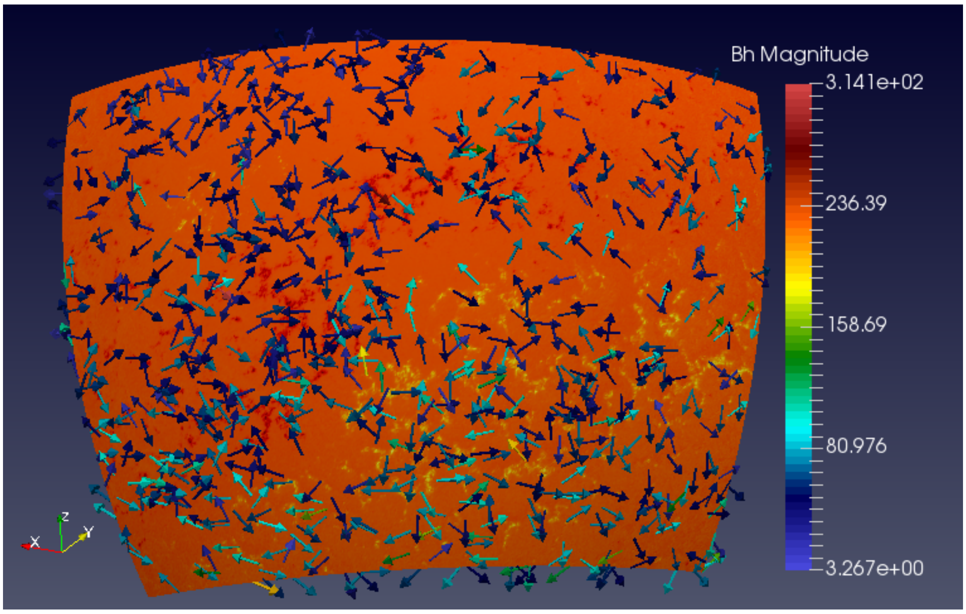

Figure 4.6: The arrows show the horizontal components of the magnetic field obtained from SDO/HMI data model after preprocessing. The color coding in the arrows show the magnitude of the horizontal components of the magnetic field in Gauss.

PFSS model to describe topological magnetic field structures of the filament. In this model the field lines over the filament do not show sheared arcades and this indicates that the model hardly demonstrates magnetic topology of the filament.

The qualitative comparison between the model magnetic field lines and the observed EUV loops indicates that the NLFFF model provides a more consistent field for the filament's magnetic field reconstruction. Figures (4.11) and (4.12) show that there is over all similarity between the corresponding NLFFF model field lines and image of the Sun observed by the SDO/AIA coronagraph.

In order to initialize the NLFFF code, we calculated potential field from HMI and VSM data sets from their respective preprocessed radial field components (B_r) using spherical harmonic expansion. This code solves the NLFFF equations in the bounded domain between $1R_{\odot}$ and the source surface at $2.5R_{\odot}$. The outer bound-

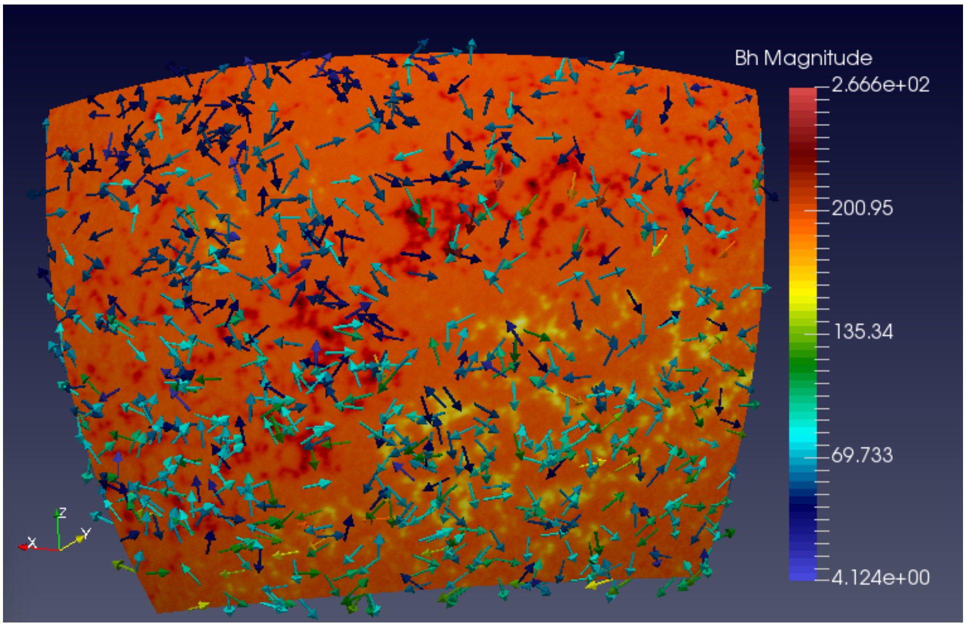

Figure 4.7: The arrows show the horizontal components of the magnetic field from SOLIS/VSM data model after preprocessing. The color coding in the arrows show the magnitude of the horizontal components of the magnetic field in Gauss.

ary is kept fixed using the initial potential field values. All current-carrying field lines have to be confined in the volume. We implement the new term L_{photo} in Eq. (3.51) to work with boundary data of different noise levels and qualities or even neglect some data points completely.

For nonlinear force-free fields we minimize the functional L_ω Eq. (3.51) . In order to control the speed with which the lower boundary is injected during the extrapolation, we vary the Lagrangian multiplier ν between 0.1 and 0.0001 to investigate the optimal parameter for HMI data. To evaluate how well the force-free and divergence-free condition are satisfied for different Lagrangian multiplier ν, we monitor a number of expressions, such as σ_j, the sine of the current weighted average angle between the magnetic field **B** and electric current density **J**, L_f and L_d. The average angle was obtained to be 28.4085^o.

The surface electric current densities of the NLFFF field models based on HMI

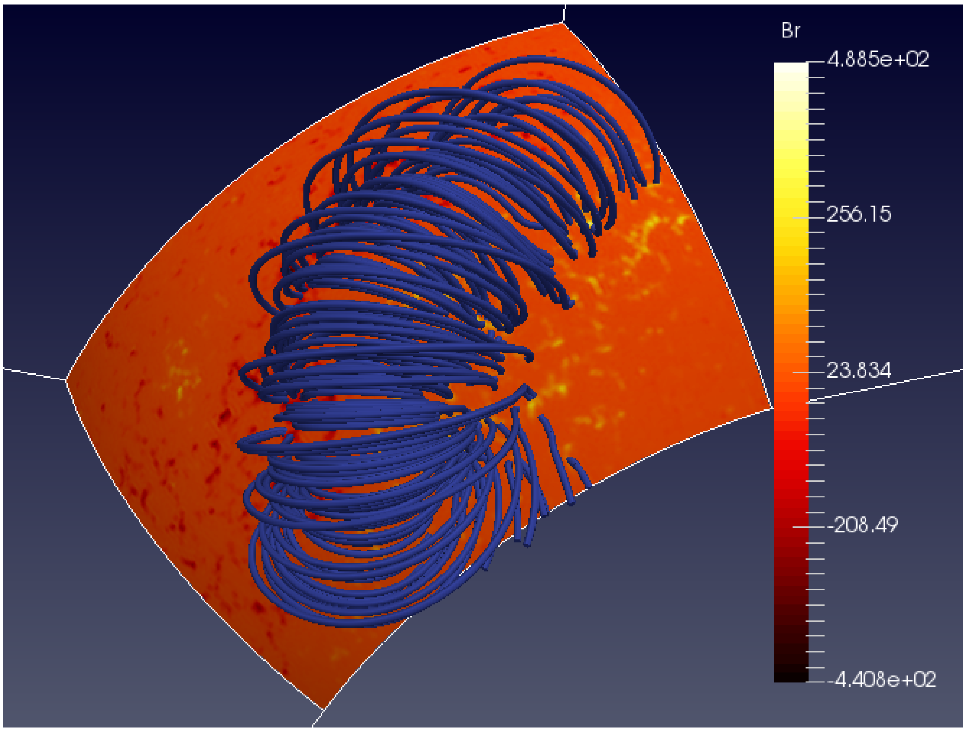

Figure 4.8: PFSS model from HMI data.

and VSM data are shown in Figures (4.9) and (4.10). The value of the total surface electric current density flux of the NLFFF field models based on HMI is greater than that of VSM. It agrees with the fact that the HMI instrument measures more magnetic field than that of VSM instrument. The surface electric current density of the NLFFF field model based on HMI spreads more around the active regions than that of VSM. This could reflect the fact that the scaling factor between SOLIS/VSM and SDO/HMI is different for weak and strong fluxes. The difference in scaling factor may act as a weighting function when comparing electric currents derived from two models.

The preprocessed NLFFF model is effective to express the full disc and large regions of coroanal magnetic field lines. For our study, the FOV is very large, so that this model can express the field structures of the filament as well. The 3D magnetic field lines over the giant filament shown in Figures (4.11) and (4.12) using SDO/HMI

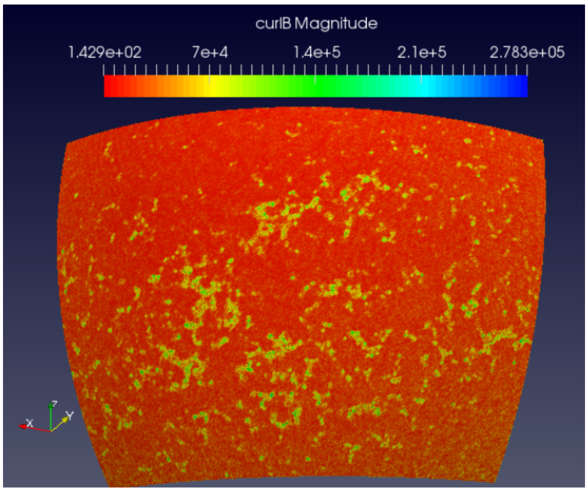

Figure 4.9: Electric current density flux distribution from SDO/HMI.

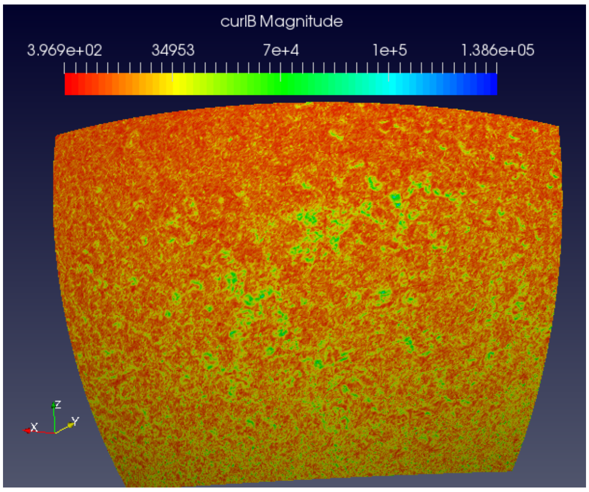

Figure 4.10: Electric current density flux distribution from SOLIS/VSM.

and SOLIS/VSM, respectively, is obtained from NLFFF IDL code to indicate magnetc field structures above the filament. The figures show that the background photospheric region has the radial magnetic field strength extends from -1.04×10^3 to 1.04×10^3 G for SDO/HMI and -8.57×10^2 to 8.32×10^2 G for the SOLIS/VSM. The magnetic field structures obtained from the model has the same position with the H_α observation indicated in Fig. (4.1) by arrow on the left hand side of the two figures. The sheared arcades both in the cases of HMI and VSM data models indicate topology of the field lines over the filament, however, twisted flux rope that support the giant filament is not clearly modeled since the filament was found in weak magnetic field region and had weak horizontal component of the magnetic field.

The magnitude of an electric current density can be obtained from the corresponding magnetic field strength of the filament region. We have found that the magnitude of the current density extends from $1.43 \times 10^1 mA/m^2$ to $2.78 \times 10^4 mA/m^2$ and from $1.43 \times 10^1 mA/m^2$ to $2.78 \times 10^4 mA/m^2$ for HMI and VSM data, respectively. The largest value indicates the highest current density in the region.

In order understand the concept of solar flares, coronal mass ejection (CME),

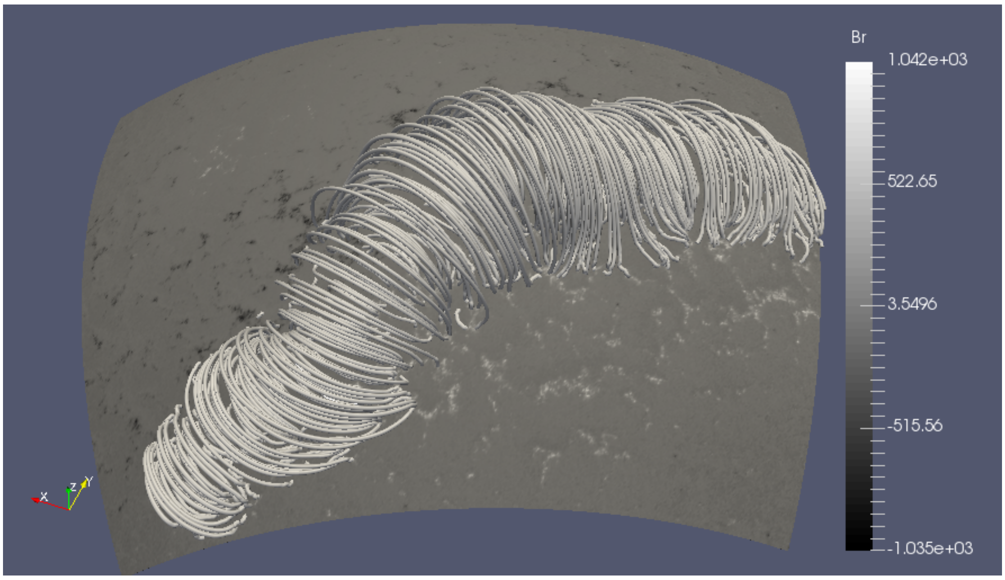

Figure 4.11: Magnetic field structures of the filament using SDO/HMI data and the background shows the radial component of the magnetic field (B_r) in Gauss.

solar filament ejection, local reorganization of magnetic field, and acceleration of energetic particles, the estimation of free magnetic energy available for these phenomena is quit important. This energy can be converted in to kinetic and thermal energy. Free energy above the minimum-energy is required for these processes to happen. For the filament region, we calculate the free magnetic energy to be the difference between the extrapolated non-linear force-free fields and the potential field with the same normal boundary conditions in the photosphere. We therefore estimate the upper limit to the free magnetic energy associated with coronal currents of the form:

$$E_{free} = \frac{1}{8\pi} \int_V \left(B^2_{NLFFF} - B^2_{PFSS} \right) r^2 sin\theta dr d\theta d\phi \tag{4.1}$$

where, B_{PFSS} and B_{NLFFF} represent the potential and NLFFF magnetic field, respectively.

Table 4.2. Magnetic energy density associated with extrapolated NLFFF field configurations from SDO/HMI and SOLIS/VSM data.

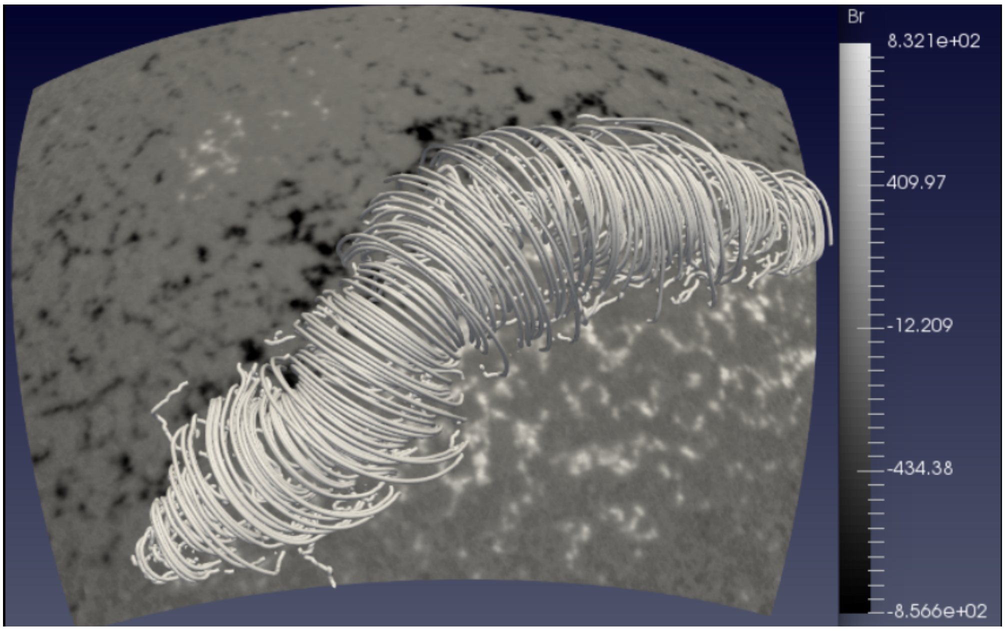

Figure 4.12: Magnetic field structures of the filament using SOLIS/VSM data and the background shows the radial component of the magnetic field (B_r) in Gauss.

Model	$U_{PFSS}(erg/cm^3)$	$U_{NLFFF}(erg/cm^3)$	$U_{free}(erg/cm^3)$	U_{NLFFF}/U_{PFSS}
SDO/HMI	1.30	2.78	1.48	2.15
SOLIS/VSM	1.70	2.35	0.65	1.38

The magnetic energy density after preprocessing is obtained for the filament region both from SDO/HMI and SOLIS/VSM data models. The magnetic energy density obtained by non-linear force-free model, U_{NLFFF} is 53.24% higher than the magnetic energy density obtained by potential field source surface model, U_{PFSS} from HMI data. Similarly, U_{NLFFF} is 27.66% higher than U_{PFSS} from VSM data. The energy density difference between U_{NLFFF} and U_{PFSS} is called a free magnetic energy density, U_{free}. The grater the free magnetic energy density the more filament eruption is observed. The ratio of magnetic energy density obtained by NLFFF model to that of magnetic energy density obtained by PFSS model is 2.14 for SDO/HMI and 2.68 for SOLIS/VSM. These results show that the NLFFF model is enough to infer topological magnetic field structure of the filament.

The free energy density obtained both from HMI and VSM data model is relatively small as compared to active region filaments and this made the filament to stay long time, about two weeks before eruption.

5

Conclusion

In this study, we have investigated magnetic field strength, electric current density, magnetic energy and topology of giant solar filament observed on February 10, 2015 by analyzing SDO/HMI and SOLIS/VSM data. We use both potetential and non-linear force-free field models and the potential field solution is used as initial condition for non-linear force-free model.

The non-linear force-free coronal field extrapolation of full-disk magnetogram have been used, and the vector magnetogram is almost flux balanced and force-free in which the field of view is enough to cover almost the whole length of the filament.

Using PFSS and NLFFF model, the following results are inferred:

• The radial component (B_r) and horizontal components (B_θ and B_ϕ) of the magnetic field strength for the filament have been obtained using SDO/HMI and SOLIS/VSM instruments. The quantitative results of both the radial and horizontal components of the magnetic field show that the filament was suspended in a weak magnetic field region.

• An electric current density of the filament is investigated both from HMI and VSM data analysis. The value of the total surface electric current density flux of the NLFFF field models based on HMI is greater than that of VSM. It agrees with the fact that the HMI instrument measures more magnetic field than that of VSM instrument.

- Reconstructing magnetic field based on SDO/HMI data have more contents of total magnetic energy density and free magnetic energy density compared to SOLIS/VSM data. The free energy is not as large as expected in the region, and this made the filament to stay about two weeks before eruption.
- The topological magnetic field structure of the filament obtained from NLFFF extrapolation based on HMI and VSM data have good correlation. The field lines show sheared arcades over the filament and follow polarity inversion line.
- The NLFFF model shows the topological magnetic field structure of the filament more accurately than the PFSS model.

In the future, we plan to study the evolution of erupting filaments which allows us to answer some basic questions: for example – how the non-equilibrium is reached leading to the eruption? What are the critical conditions for the initiation of filament eruptions that can lead to a CME? The major source of space weather problem is the physical effect of solar eruptions such as CMEs on the Earth's magnetosphere.

Moreover, I also plan to develop an effective model to study the structure and dynamics of giant filaments similar to the one in this thesis. The present models do not show the evolution of giant filaments, especially those in the weak magnetic field regions.

Bibliography

[1] Babcock, H. W. and Babcock, H. D.: 1955, ApJ **121**, 349

[2] Martin, S. F.: 1973, Sol. Phys. **31**, 3

[3] Low, B. C.: 1996, Sol. Phys. **167**, 217

[4] Lites, B. W.: 2005, ApJ **622**, 1275

[5] Tandberg-Hanssen, E., 1974, Solar Prominences, Geophysics and Astrophysics Monographs, 12, D. Reidel, Dordrecht.

[6] Hirayama, T.: 1985, Sol. Phys. **100**, 415

[7] Leroy, J. L.: 1989, in E. R. Priest (ed.), Dynamics and Structure of Quiescent Solar Prominences, Vol. 150 of Astrophysics and Space Science Library, pp 77 – 113

[8] Tandberg-Hanssen, E. (ed.): 1995, The nature of solar prominences, Vol. 199 of Astrophysics and Space Science Library

[9] Paletou, F. and Aulanier, G.: 2003, in J. Trujillo-Bueno & J. Sanchez Almeida (ed.), Astronomical Society of the Pacific Conference Series, Vol. **307** of Astronomical Society of the Pacific Conference Series, p. 458

[10] Labrosse, N., Heinzel, P., Vial, J.-C., Kucera, T., Parenti, S., Gunár, S., Schmieder, B., and Kilper, G.: 2010, Space Sci. Rev. **151**, 243

[11] Mackay, D. H., Karpen, J. T., Ballester, J. L., Schmieder, B., and Aulanier, G.: 2010, Space Sci. Rev. **151**, 333

[12] Foukal, P.V., 2004, Solar Astrophysics, Wiley-VCH, Weinheim, 2nd rev. edn. [Google Books].

[13] Secchi, A., 1870, Le Soleil, Gauthier-Villars, Paris.

[14] Lockyer, J.N., 1868, "Notice of an Observation of the Spectrum of a Solar Prominence, by J. N. Lockyer, Esq", Proc. R. Soc. London, **17**, 91–92

[15] Lyot, B., 1939, "The study of the solar corona and prominences without eclipses (George Darwin Lecture, 1939)", Mon. Not. R. Astron. Soc.,**99**, 538

[16] Bocchino, G., 1933, "Migrazione delle protuberanze durante il ciclo undecennale dell' attivitá solare ", Osserv. Mem. Oss. Astrofis. Arcetri, **51**, 5 – 47

[17] Barocas, V., 1939, "Prominences and the Sunspot Cycle", Astrophys. J., **89**, 486

[18] Tandberg-Hanssen, E.: 1998, in D. F. Webb, B. Schmieder, and D. M. Rust (ed.), IAU Colloq. 167: New Perspectives on Solar Prominences, Vol. 150 of Astronomical Society of the Pacific Conference Series, p. 11

[19] Vial, J.-C., 1998, "Solar Prominence Diagnostics (Review)" in New Perspectives on Solar Prominences, Proceedings of IAU Colloquium 167, held in Aussois, France, 28 April – 4 May 1997, (Eds.) Webb, D.F., Schmieder, B., Rust, D.M., ASP Conference Series, **150**, p. 175, Astronomical Society of the Pacific, San Francisco.

[20] Harvey, J. and Hall, D.: 1971, in R. Howard (ed.), Solar Magnetic Fields, Vol. 43 of IAU Symposium, p. 279

[21] Tsuneta, S., Ichimoto, K., Katsukawa, Y. et al., 2008, "The Solar Optical Telescope for the Hinode Mission: An Overview", Solar Phys., **249**, 167 – 196

[22] Lyot, B.: 1937, L'Astronomie **51**, 203

[23] Rust, D. M.: 1967, ApJ **150**, 313

[24] Malville, J. M.: 1968, Sol. Phys. **5**, 236

[25] Martin, S. F.: 1998, Sol. Phys. **182**, 107

[26] Malherbe, J. M., Schmieder, B., Ribes, E., and Mein, P.: 1983, A&A **119**, 197

[27] Mein, P. and Mein, N.: 1991, Sol. Phys. **136**, 317

[28] Lin, Y., Engvold, O., Rouppe van der Voort, L., Wiik, J. E., and Berger, T. E.: 2005, Sol. Phys. **226**, 239

[29] Schmieder, B., Raadu, M. A., and Wiik, J. E.: 1991, A&A **252**, 353

[30] Schmieder, B., Chandra, R., Berlicki, A., and Mein, P.: 2010, A&A **514**, A68+

[31] Smith, S. F. and Ramsey, H. E.: 1967, Sol. Phys. **2**, 158

[32] Martin, S. F.: 1998, Sol. Phys. **182**, 107

[33] Smith, S. F.: 1968, in K. O. Kiepenheuer (ed.), Structure and Development of Solar Active Regions, Vol. 35 of IAU Symposium, p. 267

[34] Foukal, P.: 1971, Sol. Phys. **19**, 59

[35] Martin, S. F.: 1990, in V. Ruzdjak & E. Tandberg-Hanssen (ed.), IAU Colloq. 117: Dynamics of Quiescent Prominences, Vol. 363 of Lecture Notes in Physics, Berlin Springer Verlag, pp 1 – 44

[36] Martin, S. F., Bilimoria, R., and Tracadas, P. W.: 1994, in R. J. Rutten & C. J. Schrijver (ed.), Solar Surface Magnetism, p. 303

[37] Martin, S. F., Lin, Y., and Engvold, O.: 2008, Sol. Phys. **250**, 31

[38] Heinzel, P. and Anzer, U., 2001, "Prominence fine structures in a magnetic equilibrium: Two-dimensional models with multilevel radiative transfer", Astron. Astrophys., **375**, 1082 – 1090

[39] Schwartz, P., Heinzel, P., Schmieder, B. and Anzer, U., 2006, "Study of an extended EUV filament using SoHO/SUMER observations of the hydrogen Lyman lines", Astron. Astrophys., **459**, 651 – 661

[40] Kippenhahn, R. and Schlüter, A.: 1957, ZAp **43**, 36

[41] Rust, D. M.: 1967, ApJ **150**, 313

[42] Kuperus, M. and Raadu, M. A.: 1974, A&A **31**, 189

[43] Tandberg-Hanssen, E. (ed.): 1995, The nature of solar prominences, Vol. 199 of Astrophysics and Space Science Library.

[44] Leroy, J. L., Bommier, V., & Sahal-Brechot, S. 1984, A&A, **131**, 33

[45] S.K. Antiochos, R.B. Dahlburg, J.A. Klimchuk, ApJ **420**, L41 (1994)

[46] Aulanier, G., DeVore, C. R., and Antiochos, S. K.: 2002, ApJ **567**, L97

[47] C.R. DeVore, S.K. Antiochos, G. Aulanier, ApJ, **629**, 1122 (2005)

[48] Mackay, D. H., Karpen, J. T., Ballester, J. L., Schmieder, B., and Aulanier, G.: 2010, Space Sci. Rev. **151**, 333

[49] Guo, Y., Schmieder, B., Démoulin, P., Wiegelmann, T., Aulanier, G., Török, T., and Bommier, V.: 2010, ApJ **714**, 343

[50] van Ballegooijen, A. A., Martens, P. C. H., 1989, Formation and eruption of solar prominences, ApJ, **343**, 971

[51] Brandt, P.N., Scharmer, G.B., Ferguson, S., Shine, R.A., Tarbell, T.D., Title, A.M., 1988, Nature, **335**, 238

[52] Browning, P.K., 1991, Plasma Phys. and Contr. Fusion, **33**, 571

[53] Van Ballegooijen, A. A. and Martens, P. C. H.: 1989, ApJ **343**, 971

[54] Fan, Y., 2010, Astrophys. J., **719**, 728

[55] Manchester, W., IV, Gombosi, T., DeZeeuw, D., and Fan, Y., 2004, Astrophys. J., **610**, 588

[56] Magara, T., 2006, Astrophys. J., **653**, 1499

[57] Parker, E.N., 1979, Cosmical magnetic fields. Their origin and their activity, Oxford.

[58] Solovev, A.A., 1985, Astrophysics, **23**, 595

[59] Okamoto, T. J., Tsuneta, S., Lites, B. W., Kubo, M., Yokoyama, T., Berger, T. E., Ichimoto, K., Katsukawa, Y., Nagata, S., Shibata, K., Shimizu, T., Shine, R. A., Suematsu, Y., Tarbell, T. D., and Title, A. M.: 2008, ApJ **673**, L215

[60] Okamoto, T. J., Tsuneta, S., Lites, B. W., Kubo, M., Yokoyama, T., Berger, T. E., Ichimoto, K., Katsukawa, Y., Nagata, S., Shibata, K., Shimizu, T., Shine, R. A., Suematsu, Y., Tarbell, T. D., and Title, A. M.: 2009, ApJ **697**, 913

[61] Martens, P. C., Zwaan, C., 2001, Origin and Evolution of Filament-Prominence Systems, ApJ, 558, 872 – 887

[62] Lites, B. W., Kubo, M., Berger, T., Frank, Z., Shine, R., Tarbell, T., Title, A., Okamoto, T. J., and Otsuji, K.: 2010, ApJ **718**, 474

[63] Xu, Z., Lagg, A., Solanki, S., and Liu, Y.: 2012, ApJ **749**, 138

[64] Fan, Y.: 2001, ApJ **554**, L111

[65] Archontis, V., Moreno-Insertis, F., Galsgaard, K., Hood, A., and O'Shea, E.: 2004, A&A **426**, 1047

[66] Magara, T.: 2004, ApJ **605**, 480

[67] Manchester, IV, W., Gombosi, T., DeZeeuw, D., and Fan, Y.: 2004, ApJ **610**, 588

[68] Murray, M. J., Hood, A. W., Moreno-Insertis, F., Galsgaard, K., and Archontis, V.: 2006, A&A **460**, 909

[69] Martínez-Sykora, J., Hansteen, V., and Carlsson, M.: 2008, ApJ **679**, 871

[70] Cheung, M. C. M., Schüssler, M., Tarbell, T. D., and Title, A. M.: 2008, ApJ **687**, 1373.

[71] Fan, Y.: 2009, ApJ **697**, 1529

[72] Yelles Chaouche, L., Cheung, M. C. M., Solanki, S. K., Schüssler, M., and Lagg, A.: 2009, A&A **507**, L53

[73] MacTaggart, D. and Hood, A. W.: 2010, ApJ **716**, L219

[74] Parker, E. N.: 1955, ApJ **121**, 491

[75] Archontis, V., Moreno-Insertis, F., Galsgaard, K., Hood, A., and OShea, E.: 2004, A&A 426, 1047

[76] MacTaggart, D. and Hood, A. W.: 2010, ApJ 716, L219

[77] Archontis, V. and Török, T.: 2008, A&A 492, L35

[78] Wang, Y.-M., 1999, The Jetlike Nature of HE II lambda304 Prominences, ApJ, **520**

[79] Chae, J., Wang, H., Qiu, J., Goode, P. R., Strous, L., Yun, H. S., 2001, The Formation of a Prominence in Active Region NOAA 8668. I. SOHO/MDI Observations of Magnetic Field Evolution, ApJ, **560**, 476 – 489

[80] J. Chae, ApJ, **584**, 1084 (2003)

[81] Y.E. Litvinenko, Sol. Phys. **196**, 369 (2000)

[82] Y.-M. Wang, ApJ **560**, 456 (2001)

[83] J. Chae, Y.-J. Moon, Y.-D. Park, ApJ, **626**, 574 (2005)

[84] J.B. Zirker, O. Engvold, Z. Yi, Sol. Phys. **150**, 81 (1994)

[85] T.E. Berger, R.A. Shine, G.L. Slater, T.D. Tarbell, A.M. Title, T.J. Okamoto, K. Ichimoto, Y. Katsukawa, Y. Suematsu, S. Tsuneta, B.W. Lites, T. Shimizu, ApJ **676**, L89 (2008)

[86] B. De Pontieu, S. W. McIntosh, M. Carlsson, V.H. Hansteen, T.D. Tarbell, et al., Science, **318**, 1574 (2007)

[87] Antiochos, S. K., Klimchuk, J. A., 1991, A model for the formation of solar prominences, ApJ, **378**, 372 – 377

[88] Antiochos, S. K., MacNeice, P. J., Spicer, D. S., 2000, The Thermal Nonequilibrium of Prominences, ApJ, **536**, 494 – 499.

[89] Karpen, J. T., Antiochos, S. K., Hohensee, M., Klimchuk, J. A., MacNeice, P. J., 2001, Are Magnetic Dips Necessary for Prominence Formation?, ApJ, **553**, L85 – L88

[90] Antiochos, S. K., MacNeice, P. J., Spicer, D. S., Klimchuk, J. A., 1999, The Dynamic Formation of Prominence Condensations, ApJ, **512**, 985 – 991

[91] Serio, S., Peres, G., Vaiana, G. S., Golub, L., Rosner, R., 1981, Closed coronal structures. II - Generalized hydrostatic model, ApJ, **243**, 288 – 300

[92] Mok, Y., Drake, J. F., Schnack, D. D., van Hoven, G., 1990, Prominence formation in a coronal loop, ApJ, **359**, 228 – 231

[93] Klimchuk, J. A., Karpen, J. T., Antiochos, S. K., 2010, Can Thermal Nonequilibrium Explain Coronal Loops?, ApJ, **714**, 1239 – 1248, 0912.0953

[94] Aschwanden, M. J., 2005, Physics of the Solar Corona. An Introduction with Problems and Solutions (2nd edition), Praxis Publishing, Chichester, UK.

[95] Trujillo Bueno, J., Asensio Ramos, A., 2007, Influence of Atomic Polarization and Horizontal Illumination on the Stokes Profiles of the HeI 10830Å Multiplet, ApJ, **655**, 642 – 650

[96] Raouafi, N., Solanki, S. K., Wiegelmann, T., 2009, Hanle Effect Diagnostics of the Coronal Magnetic Field: A Test Using Realistic Magnetic Field Configurations, vol. 405 of Astronomical Society of the Pacific Conference Series, pp. 429

[97] Solanki, S. K., Lagg, A., Woch, J., Krupp, N., Collados, M., 2003, Three-dimensional magnetic field topology in a region of solar coronal heating, Nature, **425**, 692 – 695

[98] Schmidt, H. U., 1964, On the Observable Effects of Magnetic Energy Storage and Release Connected With Solar Flares, in The Physics of Solar Flares, pp. 107

[99] Semel, M., 1967, Contribution álétude des champs magnétiques dans les régions actives solaires, Annales d'Astrophysique, **30**, 513 – 513

[100] Chiu, Y. T., Hilton, H. H., 1977, Exact Green's function method of solar force-free magnetic-field computations with constant alpha. I - Theory and basic test cases, ApJ, **212**, 873 – 885

[101] Seehafer, N., 1978, Determination of constant alpha force-free solar magnetic fields from magnetograph data, Sol. Phys., **58**, 215 – 223

[102] Sakurai, T., 1981, Calculation of Force-Free Magnetic Field with Non Constant Alpha, Sol. Phys., **69**, 343

[103] Seehafer, N., 1982, A comparison of different solar magnetic field extrapolation procedures, Sol. Phys., **81**, 69 – 80

[104] Semel, M., 1988, Extrapolation functions for constant-alpha force-free fields — Green's method for the oblique boundary value, A&A, **198**, 293 – 299

[105] Wu, S. T., Sun, M. T., Chang, H. M., Hagyard, M. J., Gary, G. A., 1990, On the numerical computation of nonlinear force-free magnetic fields, ApJ, **362**, 698 – 708

[106] Cuperman, S., Demoulin, P., Semel, M., 1991, Removal of singularities in the Cauchy problem for the extrapolation of solar force-free magnetic fields, A&A, **245**, 285 – 288

[107] Demoulin, P., Cuperman, S., Semel, M., 1992, Determination of force-free magnetic fields above the photosphere using three-component boundary conditions. II - Analysis and minimization of scale-related growing modes and of computational induced singularities, A&A, **263**, 351 – 360

[108] Mikic, Z., McClymont, A. N., 1994, Deducing Coronal Magnetic Fields from Vector Magnetograms, in Solar Active Region Evolution: Comparing Models with Observations, (Eds.) K. S. Balasubramaniam, G. W. Simon, vol. 68 of Astronomical Society of the Pacific Conference Series, pp. 225

[109] Roumeliotis, G., 1996, The "Stress-and-Relax" Method for Reconstructing the Coronal Magnetic Field from Vector Magnetograph Data, ApJ, **473**, 1095

[110] Amari, T., Aly, J. J., Luciani, J. F., Boulmezaoud, T. Z., Mikic, Z., 1997, Reconstructing the Solar Coronal Magnetic Field as a Force-Free Magnetic Field, Sol. Phys., **174**, 129 – 149

[111] Amari, T., Boulmezaoud, T. Z., Mikic, Z., 1999, An iterative method for the reconstruction break of the solar coronal magnetic field. I. Method for regular solutions, A&A, **350**, 1051 – 1059

[112] Clegg, J. R., Browning, P. K., Laurence, P., Bromage, B. J. I., Stredulinsky, E., 2000, The linear force-free field in a spherical shell using a new method to determine the coefficients of the eigenfunction expansion, A&A, **361**, 743 – 758

[113] Wheatland, M. S., Sturrock, P. A., Roumeliotis, G., 2000, An Optimization Approach to Reconstructing Force-free Fields, ApJ, **540**, 1150 – 1155

[114] Yan, Y., Sakurai, T., 2000, New Boundary Integral Equation Representation for Finite Energy Force-Free Magnetic Fields in Open Space above the Sun, Sol. Phys., **195**, 89 – 109

[115] Wheatland, M. S., 2004, Parallel Construction of Nonlinear Force-Free Fields, Sol. Phys., **222**, 247 – 264

[116] Wiegelmann, T., 2004, Optimization code with weighting function for the reconstruction of coronal magnetic fields, Sol. Phys.,**219**, 87 – 108

[117] Valori, G., Kliem, B., Keppens, R., 2005, Extrapolation of a nonlinear force-free field containing a highly twisted magnetic loop, A&A, **433**, 335 – 347

[118] Neukirch, T., 2005, Magnetic Field Extrapolation, in Chromospheric and Coronal Magnetic Fields, (Ed.) D. E. Innes, A. Lagg, & S. A. Solanki, vol. 596 of ESA Special Publication.

[119] Amari, T., Boulmezaoud, T. Z., Aly, J. J., 2006, Well posed reconstruction of the solar coronal magnetic field, A&A, **446**, 691 – 705

[120] Wiegelmann, T., 2007, Computing Nonlinear Force-Free Coronal Magnetic Fields in Spherical Geometry, Sol. Phys., **240**, 227 – 239

[121] Tadesse, T., Wiegelmann, T., Inhester, B., 2009, Nonlinear force-free coronal magnetic field modelling and preprocessing of vector magnetograms in spherical geometry, A&A, **508**, 421 – 432

[122] DeRosa, M. L., Schrijver, C. J., Barnes, G., Leka, K. D., Lites, B. W., Aschwanden, M. J., Amari, T., Canou, A., McTiernan, J. M., Régnier, S., Thalmann, J. K., Valori, G., Wheatland, M. S., Wiegelmann, T., Cheung, M. C. M., Conlon, P. A., Fuhrmann, M., Inhester, B., Tadesse, T., 2009, A Critical Assessment of Nonlinear Force-Free Field Modeling of the Solar Corona for Active Region 10953, ApJ, **696**, 1780 –1791

[123] Wheatland, M. S., Régnier, S., 2009, A Self-Consistent Nonlinear Force-Free Solution for a Solar Active Region Magnetic Field, ApJL, **700**, L88 – L91

[124] Tadesse, T., 2011, Nonlinear force-free reconstruction of the coronal magnetic field with advanced numerical methods, ISBN 978-3-942171-45-8

[125] Landi Degl'Innocenti, E.: 1992, Magnetic field measurements, pp 71-+

[126] Del Toro Iniesta, J. C.: 2003, Introduction to Spectropolarimetry.

[127] Casini, R. and Manso Sainz, R. J.Phys.B: At.Mol.Opt.Phys. **39**, 3241 (2006)

[128] Stix, M.: 2002, The sun: an introduction.

[129] Trujillo Bueno, J.: 2006, in R. Ramelli, O. Shalabiea, I. Saleh, & J. O. Stenflo (ed.), Solar Physics and Solar Eclipses (SPSE 2006), pp 77 – 92

[130] Trujillo Bueno, J., Casini, R., Landolfi, M., and Landi DeglInnocenti, E., The Physical Origin of the Scattering Polarization of the NaI D Lines in the Presence of Weak Magnetic Fields, ApJL, **566**, L53 (2002a). doi:10.1086/339442

[131] Trujillo Bueno, J., Shchukina, N., and Asensio Ramos, A., A substantial amount of hidden magnetic energy in the quiet Sun, Nature, **430**, 326 (2004). doi:10.1038/nature02669

[132] Stein, R.F., & Nordlund, Å. 1998, ApJ, **499**, 914

[133] Asplund, M., Nordlund, Å., Trampedach, R., Allende-Prieto, C., & Stein, R.F. 2000, A&A, **359**, 729

[134] Shchukina, N., & Trujillo Bueno, J. 2001, ApJ, **550**, 970

[135] Socas-Navarro, H. 2001, in Advanced Solar Polarimetry-Theory, Observation, and Instrumentation, ed. M. Sigwarth, ASP Conf. Ser., **236**, 487

[136] Del Toro Iniesta, J. C. 2003a, Astron. Nachr., **324**, 383

[137] Rubio, L. R. 2006, in ASP Conf. Ser. 358, eds. R. Casini,& B. W. Lites, 107

[138] Ruiz Cobo, B. 2007, in Modern solar facilities — advanced solar science, Proc. of a Workshop held at Göttingen, eds. F. Kneer, K. G. Puschmann, & A. D. Wittmann, 287

[139] Liu, Y., Hoeksema, J. T., Scherrer, P. H., et al. 2012, Sol. Phys., **279**, 295

[140] Couvidat, S., Rajaguru, S. P., Wachter, R., et al. 2012, Sol. Phys., **278**, 217

[141] Schlichenmaier, R., Bellot Rubio, L. R., & Tritschler, A. 2004, A&A, **415**, 731

[142] Franz, M., & Schlichenmaier, R. 2013, A&A, **550**, A97

[143] Balthasar, H., & Schmidt, W. 1993, A&A, **279**, 243

[144] Penn, M. J., & Livingston, W. 2006, ApJ, **649**, L45

[145] Jefferies, J. T., & Mickey, D. L. 1991, ApJ, **372**, 694

[146] Lites, B., Casini, R., Garcia, J., & Socas-Navarro, H. 2007, Mem. Soc. Astron. It., **78**, 148

[147] Borrero, J. M., Tomczyk, S., Kubo, M., et al. 2011, Sol. Phys., **273**, 267

[148] Keller, C. U., Harvey, J. W., & Solis Team 2003, in Solar Polarization, eds.

[149] Auer, L. H., House, L. L., & Heasley, J. N. 1977, Sol. Phys., **55**, 47

[150] Lagg, A. 2007, Adv. Space Res.,**39**, 1734

[151] Gary, G.A. and Hagyard, M.J., 1990, “Transformation of vector magnetograms and the problems associated with the effects of perspective and the azimuthal ambiguity”, Solar Phys., **126**, 21 – 36.

[152] Harvey, J. W., 1969, Magnetic Fields Associated with Solar Active-Region Prominences., Ph.D. thesis, University of Colorado at Boulder.

[153] Metcalf, T. R., Leka, K. D., Barnes, G., Lites, B. W., Georgoulis, M. K., Pevtsov, A. A., Balasubramaniam, K. S., Gary, G. A., Jing, J., Li, J., Liu, Y., Wang, H. N., Abramenko, V., Yurchyshyn, V., and Moon, Y.-J.: 2006, Sol. Phys. **237**, 267

[154] Wang, H., 1997, "Distribution of 2-D magnetic saddle points and morphology of flare kernels in solar active regions", Solar Phys., **174**, 265 – 279

[155] Wang, H., Yan, Y. and Sakurai, T., 2001, "Topology of magnetic field and coronal heating in solar active regions“, Solar Phys., **201**, 323 – 336

[156] Metcalf, T. R.: 1994, Sol. Phys. **155**, 235

[157] Cuperman, S., Li, J. and Semel, M., 1993, ”Identification and elimination of the residual ambiguity in the sign of observed photospheric magnetic fields“, Astron. Astrophys., **278**, 279 – 287

[158] Moon, Y.-J., Wang, H., Spirock, T. J., Goode, P. R., and Park, Y. D.: 2003, Sol. Phys. **217**, 79

[159] Georgoulis, M. K., LaBonte, B. J., and Metcalf, T. R.: 2004, ApJ **602**, 446

[160] Lites, B. W., Low, B. C., Martinez Pillet, V., Seagraves, P., Skumanich, A., Frank, Z. A., Shine, R. A., and Tsuneta, S.: 1995, ApJ **446**, 877

[161] Martin, S. F., Lin, Y., and Engvold, O.: 2008, Sol. Phys. **250**, 31

[162] Metcalf, T. R. 1994, Sol. Phys., **155**, 235

[163] Metcalf, T. R., Leka, K. D., Barnes, G., et al. 2006, Sol. Phys., **237**, 267

[164] Jing, J., Yuan, Y., Wiegelmann, T., Xu, Y., Liu, R., and Wang, H.: 2010, ApJ **719**, L56

[165] Pesnell, W. D., Thompson, B. J., Chamberlin, P. C., 2012, The Solar Dynamics Observatory (SDO), Solar Phys., **275**, 3 – 15

[166] Lemen, J. R., Title, A. M., Akin, D. J., Boerner, P. F., Chou, C., Drake, J. F., Duncan, D. W., Edwards, C. G., Friedlaender, F. M., Heyman, G. F., Hurlburt, N. E., Katz, N. L., Kushner, G. D., Levay, M., Lindgren, R. W., Mathur, D. P., McFeaters, E. L., Mitchell, S., Rehse, R. A., Schrijver, C. J., Springer, L. A., Stern, R. A., Tarbell, T. D., Wuelser, J.-P., Wolfson, C. J., Yanari, C., Bookbinder, J. A., Cheimets, P. N., Caldwell, D., Deluca, E. E., Gates, R., Golub, L., Park, S., Podgorski, W. A., Bush, R. I., Scherrer, P. H., Gummin, M. A., Smith, P., Auker, G., Jerram, P., Pool, P., Soufli, R., Windt, D. L., Beardsley, S., Clapp, M., Lang, J., Waltham, N., 2012, The Atmospheric Imaging Assembly (AIA) on the Solar Dynamics Observatory (SDO), Solar Phys., **275**, 17 – 40

[167] Podgorski, W. A., Cheimets, P. N., Boerner, P., Glenn, P., 2009, SDO-AIA mirror performance, in Society of Photo-Optical Instrumentation Engineers (SPIE) Conference Series, vol. 7438 of Society of Photo-Optical Instrumentation Engineers (SPIE) Conference Series.

[168] Cheimets, P., Caldwell, D. C., Chou, C., Gates, R., Lemen, J., Podgorski, W. A., Wolfson, C. J., Wuelser, J.-P., 2009, SDO-AIA telescope design, in Society of Photo-Optical Instrumentation Engineers (SPIE) Conference Series, vol. 7438 of Society of Photo-Optical Instrumentation Engineers (SPIE) Conference Series.

[169] Boerner, P., Edwards, C., Lemen, J., Rausch, A., Schrijver, C., Shine, R., Shing, L., Stern, R., Tarbell, T., Title, A., Wolfson, C. J., Soufli, R., Spiller, E., Gullikson, E., McKenzie, D., Windt, D., Golub, L., Podgorski, W., Testa, P., Weber, M., 2012, Initial Calibration of the Atmospheric Imaging Assembly (AIA) on the Solar Dynamics Observatory (SDO), Solar Phys., **275**, 41 – 66

[170] Scherrer, P. H., Schou, J., Bush, R. I., Kosovichev, A. G., Bogart, R. S., Hoeksema, J. T., Liu, Y., Duvall, T. L., Zhao, J., Title, A. M., Schrijver, C. J., Tarbell, T. D., Tomczyk, S., 2012, The Helioseismic and Magnetic Imager (HMI) Investigation for the Solar Dynamics Observatory (SDO), Solar Phys., **275**, 207 – 227

[171] Schou, J., Borrero, J.M., Norton, A.A., Tomczyk, S., Elmore, D., Card, G.L.: 2012b, Polarization Calibration of the Helioseismic and Magnetic Imager (HMI) Onboard the Solar Dynamics Observatory (SDO). Solar Phys. **275**, 327 – 355

[172] Woods, T. N., Hock, R., Eparvier, F., Jones, A. R., Chamberlin, P. C., Klimchuk, J. A., Didkovsky, L., Judge, D., Mariska, J., Warren, H., Schrijver, C. J., Webb, D. F., Bailey, S., Tobiska, W. K., 2011, New Solar Extreme-ultraviolet Irradiance Observations during Flares, ApJ, **739**, 59

[173] C. U. Keller, J. W. Harvey, M. S. Giampapa, "SOLIS: an innovative suite of synoptic instruments", Society of Photo-Optical Instrumentation Engineers (SPIE) Conference Series, vol. 4853, pp. 194 – 204 (2003)

[174] L. Bertello, A. A. Pevtsov, J. W. Harvey, J. W., R. M. Toussaint, "Improvements in the determination of ISS CaII K parameters," Solar Physics, in press (2011).

[175] Borrero, J. M., Tomczyk, S., Kubo, M., et al. 2011, Sol. Phys., **273**, 267

[176] Turmon, M., Jones, H. P., Malanushenko, O. V., & Pap, J. M. 2010, Sol. Phys., **262**, 277

[177] Leka, K. D., Barnes, G., Crouch, A. D., et al. 2009, Sol. Phys., **260**, 83

[178] Ronan, R. S., Mickey, D. L., Orrall, F. Q. 1987, Sol. Phys., **113**, 353

[179] Unno, W. 1956, Publ. Astron. Soc. Japan, **8**, 108

[180] Skumanich, A. Lites, B. W. 1987, ApJ, **322**, 473

[181] Georgoulis, M. K. 2005, ApJL, **629**, L69

[182] Schatten, K.H., Wilcox, J.M. and Ness, N.F., 1969, "A model of interplanetary and coronal magnetic fields", Solar Phys., **6**, 442 – 455

[183] Sakurai, T., 1989, Computational modeling of magnetic fields in solar active regions, Space Sci. Rev., **51**, 11 – 48

[184] Amari, T., Luciani, J. F., Aly, J. J., Tagger, M., 1996, Very Fast Opening of a Three-dimensional Twisted Magnetic Flux Tube, ApJL, **466**, L39

[185] Mikic, Z., Linker, J. A., Schnack, D. D., 1996, Modeling of Active-Region Magnetic Fields, in Solar Drivers of the Interplanetary and Terrestrial Disturbances, (Ed.) K. S. Balasubramaniam, S. L. Keil, & R. N. Smartt, vol. 95 of Astronomical Society of the Pacific Conference Series, pp. 108

[186] Wang, Y., Sheeley, Jr., N. R., 1990, Magnetic flux transport and the sunspot-cycle evolution of coronal holes and their wind streams, ApJ, **365**, 372 – 386

[187] Hoeksema, J. T., 1991, Large-scale solar and heliospheric magnetic fields, Adv. Space Res., **11**, 15 – 24

[188] Schrijver, C. J., De Rosa, M. L., 2003, Photospheric and heliospheric magnetic fields, Sol. Phys., **212**, 165 – 200

[189] Sakurai, T., 1979, A New Approach to the Force-Free Field and Its Application to the Magnetic Field of Solar Active Regions, Publ. Astron. Soc. Japan, **31**, 209 – 230

[190] Jackson, J. D., 1975, Classical electrodynamics, New York: Wiley, 2nd ed.

[191] Nakagawa, Y., Raadu, M. A., 1972, On Practical Representation of Magnetic Field, Sol. Phys., **25**, 127 – 135

[192] Seehafer, N., 1978, Determination of constant alpha force-free solar magnetic fields from magnetograph data, Sol. Phys., **58**, 215 – 223

[193] Wiegelmann, T., 2008, Nonlinear force-free modeling of the solar coronal magnetic field, J. Geophys. Res., 113, 3

[194] Schrijver, C. J., De Rosa, M. L., Metcalf, T. R., Liu, Y., McTiernan, J., Régnier, S., Valori, G., Wheatland, M. S., and Wiegelmann, T.: 2006, Sol. Phys. **235**, 161

[195] Yan, Y., Deng, Y., Karlický, M., Fu, Q., Wang, S., and Liu, Y.: 2001, ApJ **551**, L115

[196] Guo, Y., Schmieder, B., Démoulin, P., Wiegelmann, T., Aulanier, G., Török, T., and Bommier, V.: 2010, ApJ **714**, 343

[197] Canou, A. and Amari, T.: 2010, ApJ **715**, 1566

[198] Jing, J., Yuan, Y., Wiegelmann, T., Xu, Y., Liu, R., and Wang, H.: 2010, ApJ **719**, L56

[199] Metcalf, T. R., Derosa, M. L., Schrijver, C. J., Barnes, G., van Ballegooijen, A. A., Wiegelmann, T., Wheatland, M. S., Valori, G., McTtiernan, J. M., 2008, Nonlinear Force-Free Modeling of Coronal Magnetic Fields. II. Modeling a Filament Arcade and Simulated Chromospheric and Photospheric Vector Fields, Sol. Phys., **247**, 269 – 299

[200] Schrijver, C.J., DeRosa, M.L., Metcalf, T., Barnes, G., Lites, B.W., Tarbell, T.D., McTiernan, J., Valori, G., Wiegelmann, T., Wheatland, M.S., Amari, T., Aulanier, G., Démoulin, P., Fuhrmann, M., Kusano, K., Régnier, S. and Thalmann, J.K., 2008, ”Nonlinear force-free field modeling of a solar active region around the time of a major flare and coronal mass ejection“, Astrophys. J., **675**, 1637 – 1644.

[201] DeRosa, M.L., Schrijver, C.J., Barnes, G., Leka, K.D., Lites, B.W., Aschwanden, M.J., Amari, T., Canou, A., McTiernan, J.M., Régnier, S., Thalmann, J.K., Valori, G., Wheatland, M.S., Wiegelmann, T., Cheung, M.C.M., Conlon, P.A., Fuhrmann, M., Inhester, B. and Tadesse, T., 2009, ”A Critical Assessment of Nonlinear Force-Free Field Modeling of the Solar Corona for Active Region 10953“, Astrophys. J., **696**, 1780 – 1791

[202] Gary, G.A., 2001, ”Plasma beta above a solar active region: Rethinking the paradigm“, Solar Phys., **203**, 71 – 86

[203] Yelles Chaouche, C. Kuckein, V. Martnez Pillet, and F. Moreno-Insertis. The Three-dimensional Structure of an Active Region Filament as Extrapolated from Photospheric and Chromospheric Observations. Astrophys. J., 748:23, Mar. 2012.

[204] Wiegelmann, T., Inhester, B., Sakurai, T., 2006, Preprocessing of vector magnetograph data for a nonlinear force-free magnetic field reconstruction., Sol. Phys.,**233**, 215 – 232

[205] Molodensky, M. M., 1969, Integral properties of force-free fields, Soviet Astron.-AJ, **12**, 585 – 588

[206] Aly, J. J., 1984, On some properties of force-free magnetic fields in infinite regions of space, ApJ, **283**, 349362

[207] Low, B. C., 1985, Modeling solar magnetic structures., NASA Conference Publication, **2374**, 49 – 65

[208] Sakurai, T., 1994, Integrated Force-Balance Equations for the Magnetic Field in Spherical Geometry, in Solar Active Region Evolution: Comparing Models with Observations, (Eds.) K. S. Balasubramaniam, G. W. Simon, vol. 68 of Astronomical Society of the Pacific Conference Series, pp. 307

[209] Aly, J. J., 1988, Some properties of the solutions of a non-linear boundary value problem for a force-free field in an infinite region of space. I - Energy estimates, A&A, **203**, 183 – 188

[210] Wheatland, M. S., Sturrock, P. A., & Roumeliotis, G. 2000, ApJ, **540**, 1150

[211] Wiegelmann, T. 2004, Sol. Phys.,**219**, 87

[212] Wiegelmann, T. 2007, Sol. Phys.,**240**, 227

[213] Wiegelmann, T. & Inhester, B. 2010, A&A, **516**, A107+

[214] Wiegelmann, T., Thalmann, J. K., Inhester, B., et al. 2012, Sol. Phys., **67**

Declaration

I hereby declare that except where specific reference is made to the work of others, the contents of this dissertation are original and have not been submitted in whole or in part for consideration for any other degree or qualification in this, or any other university. This dissertation is my own work and contains nothing which is the outcome of work done in collaboration with others, except as specified in the text and Acknowledgements.

Name: Abbi Seyoum

Signature: ____________

This PhD dissertation has been submitted for examination with my approval as University advisor.

Name: Dr. Araya Asfaw

Signature: ______________

Place and date of submission:

Department of Physics

Addis Ababa University

June 2018